

Binary neutron star mergers with SPHINCS_BSSN: temperature-dependent equations of state and damping of constraint violations

Bhaskar Biswas^{1,2}, Stephan Rosswog^{1,2}, Peter Diener^{3,4}, Lukas Schnabel¹

¹*Hamburger Sternwarte, Gojenbergsweg 112, D-21029 Hamburg, Germany,*

²*The Oskar Klein Centre, Department of Astronomy, Stockholm University, AlbaNova, SE-10691 Stockholm, Sweden,*

³*Center for Computation & Technology, Louisiana State University, 70803, Baton Rouge, LA, USA,*

⁴*Department of Physics & Astronomy, Louisiana State University, 70803, Baton Rouge, LA, USA*

Neutron star mergers hold the key to several grand challenges of contemporary (astro-)physics. In view of the upcoming next generation of ground-based detectors, it is crucial to keep improving theoretical predictions to harvest the full scientific returns from these investments. We introduce here a substantial update of our Lagrangian numerical relativity code **SPHINCS_BSSN**. Apart from changing our unit system, we add constraint damping terms to the BSSN spacetime evolution equations. We demonstrate that this measure reduces, without noteworthy computational cost, the Hamiltonian constraint violations by more than an order of magnitude. We further implement contributions to thermal energy and pressure that are based on Fermi liquid theory and contain a parametrization of the Dirac effective mass. These terms can be combined with any cold equation of state, and they enhance the physical realism of our simulations and introduce a physics-based concept of a temperature. In a set of merger simulations, we demonstrate good agreement with other temperature-dependent numerical relativity simulations. We find that different parametrizations of the Dirac effective mass can translate into shifts of ~ 150 Hz in the dominant post-merger gravitational wave peak frequency.

I. INTRODUCTION

The merger process of two neutron stars is shaped by physics under the most extreme conditions, involving strongly curved and dynamically changing spacetimes [1–5] with potential black hole (BH) formation, matter densities exceeding several times nuclear matter density [6, 7], magnetic fields that are locally amplified to mind-boggling field strengths [8–17], and neutrino emission at luminosities that, for short times, exceed the solar photon luminosity by 20 orders of magnitude [18–22].

Although the extreme-physics environment is interesting in its own right, neutron star mergers are also closely related to many other grand challenges of contemporary physics and astrophysics, including dark matter questions [23–26], deviations from GR [27, 28], or the properties of hot and dense nuclear matter [29–31] that may leave imprints on the post-merger GW signal [32]. Neutron star mergers have been suggested as sources of heavy elements for a long time [33–36] and, as of today, they are the only confirmed cosmic source of r-process elements [37–41]. Moreover, neutron star mergers can power short and possibly even long gamma ray bursts [42–47] and they are “standard sirens” that offer an alternative Hubble parameter estimation [48–50].

To make significant progress on these challenging questions requires the comparison of signatures of several messengers, ideally gravitational and electromagnetic waves and neutrinos, with theoretical models. Thus, there is a strong impetus to continuously improve on the physics and numerics of neutron star merger models.

While numerical relativity is traditionally performed with Eulerian methods [1–5], we have recently begun to develop an alternative methodology where we use well-established mesh-based methods for the evolution of the

spacetime, but we use Lagrangian particles to evolve the fluid [51–53]. This methodology is implemented in the **SPHINCS_BSSN** code [54]. The ejecta of neutron star mergers are only about $\sim 1\%$ of the binary mass, but their exact properties are crucial for multi-messenger astrophysics, since they shape the whole electromagnetic emission. Lagrangian methods have major advantages when it comes to following merger ejecta: advection is exact (i.e. a particle carries matter properties such as the electron fraction without any loss of information while in a Eulerian method this is subject to resolution), and the particle nature provides naturally “fluid tracers” without any need for additional computational infrastructure. Moreover, the particle motion is not restricted by grid boundaries and can, in principle, be followed out to infinity. As an example, in the (essentially Newtonian) simulations of [55] the ejecta were followed up to 100 years post-merger.

The **SPHINCS_BSSN** code [54] has been written from scratch and in its original version solved the BSSN equations [1–5] on a uniform mesh and used a polytropic equation of state. These ingredients allowed for a comparison with the tests that were performed in the pioneering Eulerian numerical relativity simulations. We found generally excellent agreement with results from the literature, for example, for the challenging “migration test” where an unstable neutron star, depending on the initial perturbation, transitions [56–58], either 1) to a wildly oscillating neutron star or 2) it collapses into a BH. We also found excellent agreement with the literature in terms of the frequencies of oscillating neutron stars [54, 59]. In the latter publication, we found that the first five harmonics of an oscillating neutron star agreed to sub-percent precision with the results from perturbation codes.

In the first **SPHINCS_BSSN** implementation, the en-

ergy momentum tensor at the particle positions was mapped to the spacetime mesh via high-accuracy kernels borrowed from vortex methods [60]. In the first paper discussing neutron star merger simulations with `SPHINCS_BSSN` [61] we used a (fixed in time) mesh-refinement. In this paper we further improved the accuracy of the mapping between the particles and the mesh, and we translated the “artificial pressure method” [62], originally designed to create high-accuracy Newtonian SPH initial conditions, to general relativity. In a companion paper [63] we introduced piecewise polytropic approximations to nuclear physics-based equations of state in `SPHINCS_BSSN` and we approximated thermal effects as an ideal-gas law with a thermal exponent Γ_{th} . We applied this new methodology to simulate binary neutron star mergers with different equations of state and we explored their gravitational wave emission and the impact of the thermal exponent Γ_{th} , e.g. on the dynamically ejected matter.

The next major code update, `SPHINCS_BSSN_v1.0`, is documented in [64]. It contains a further improvement of the particle-to-mesh mapping via a local regression estimate (LRE) coupled with a “multi-dimensional optimal order detection” (MOOD) algorithm and it allows dynamical refinement of the spacetime mesh to robustly follow neutron stars that collapse into BHs. The astrophysical applications of `SPHINCS_BSSN_v1.0` so far contain the study of the multi-messenger signatures of neutron star mergers where only one of the two stars is rapidly spinning [65]. This scenario should be realized in $\sim 5\%$ of the merging binaries. Another application was the exploration of fast ejecta in a neutron star merger [66], where, enabled by the Lagrangian nature of `SPHINCS_BSSN`, we identified two different mechanisms to eject semi-relativistic matter ($v > 0.5c$).

In the present paper, we describe three new developments in `SPHINCS_BSSN`. First, we give up on our original convention to measure all energies in terms of the nucleon rest mass energy m_0c^2 . While this convention makes the basic hydrodynamic equations look very clean and in particular makes the baryon number conservation very transparent, it makes it difficult to add new physics because of the somewhat involved units. Second, we improve our spacetime evolution equations. So far we have followed the standard BSSN approach, where one starts from constraint-satisfying initial conditions and then evolves the BSSN variables forward in time and monitors possible constraint violations, but without trying to suppress such violations. Now, we add additional constraint-damping terms to our BSSN formulation where we closely follow the suggestions that Etienne [67] made in the Eulerian context. Last but not least, we improve on our treatment of thermal effects in the equation of state. Instead of using a fixed thermal Γ_{th} , we use contributions to pressure and thermal energy that are based on Fermi liquid theory, e.g. [29, 68, 69]. Here we follow closely the work of Raithel et al. [70, 71] that have followed such an approach in the Eulerian context.

Apart from enhancing the physical realism of the equation of state, this approach also provides a physics-based temperature that is needed, for example, for neutrino reactions.

Our paper is structured as follows. In the first part of Sec. II we concisely summarize the hydrodynamics equations, now *without* the convention of measuring all energies in units of m_0c^2 . In the second part, we summarize our constraint damping procedure and in the third part the thermal equation of state (EOS), that can be combined with any cold matter EOS, is explained in detail. In Sec. III, we demonstrate the effects of constraint damping and of the thermal EOS before we conclude in Sec. IV.

II. IMPROVED METHODOLOGY

This paper introduces three new elements in the `SPHINCS_BSSN` simulation methodology: new conventions in formulating the equations, additional constraint damping terms for the spacetime evolution and physics-based thermal contributions in the equation of state that are based on Fermi liquid theory [72].

A. General relativistic Hydrodynamics with `SPHINCS_BSSN`

In our previous work related to `SPHINCS_BSSN` we have always followed the convention to measure all forms of energy in terms of the nucleon rest mass energy m_0c^2 , since this makes the equations very elegant and the conservation of nucleon number particularly transparent. The resulting units, however, are somewhat cumbersome. Therefore, we give up on this convention here, so that our new units are exactly the same as the standard units used in numerical relativity codes with $G = c = 1$. The derivation of the SPH equations can be found in explicit detail in [52, 73] and, in more concise form in [53, 59, 74].

Explicitly, the changes are the following: what we so far called “baryon number density measured in the computing frame”, N , now becomes mass density in the computing frame, $\rho^* = m_0N$, where m_0 is the baryon mass¹ and what we, so far, used as “pressure” was actually pressure in units of m_0c^2 (since it has dimensions of an energy density). Giving up our previous m_0c^2 convention and ignoring the grad-h terms (derived for the general relativistic case in [73]), our GR SPH equations in a fixed

¹ In principle, the average baryonic mass depends on the exact composition. In practice, however, deviations from the atomic mass unit are even in the worst case much smaller than 1%, see Sec. 2.1.1 in [61]. Therefore, we use the numerical value of the atomic mass unit for m_0 .

computing frame read

$$\rho_a^* = \sum_b m_b W_{ab}(h_a) \quad (1)$$

$$\left(\frac{dS_i}{dt} \right)_a = \left(\frac{d(S_i)_a}{dt} \right)_{\text{hyd}} + \left(\frac{d(S_i)_a}{dt} \right)_{\text{met}} \quad (2)$$

$$\frac{de_a}{dt} = \left(\frac{de_a}{dt} \right)_{\text{hyd}} + \left(\frac{de_a}{dt} \right)_{\text{met}}, \quad (3)$$

where the hydrodynamic contributions read

$$\left(\frac{d(S_i)_a}{dt} \right)_{\text{hyd}} = - \sum_b m_b \left[\frac{P_a}{\rho_a^{*2}} D_i^a + \frac{P_b}{\rho_b^{*2}} D_i^b \right] \quad (4)$$

$$\left(\frac{de_a}{dt} \right)_{\text{hyd}} = - \sum_b m_b \left[\frac{P_a v_b^i}{\rho_a^{*2}} D_i^a + \frac{P_b v_a^i}{\rho_b^{*2}} D_i^b \right], \quad (5)$$

with

$$D_i^a \equiv \frac{\sqrt{-g_a} \partial W_{ab}(h_a)}{\partial x_a^i} \text{ and } D_i^b \equiv \frac{\sqrt{-g_b} \partial W_{ab}(h_b)}{\partial x_a^i}. \quad (6)$$

The metric terms read

$$\left(\frac{d(S_i)_a}{dt} \right)_{\text{met}} = \left(\frac{\sqrt{-g}}{2\rho^*} T^{\mu\nu} \frac{\partial g_{\mu\nu}}{\partial x^i} \right)_a \quad (7)$$

and

$$\left(\frac{de_a}{dt} \right)_{\text{met}} = - \left(\frac{\sqrt{-g}}{2\rho^*} T^{\mu\nu} \frac{\partial g_{\mu\nu}}{\partial t} \right)_a. \quad (8)$$

Note that we have made the *choice* to calculate ρ^* via a summation approach, because the combination of positive masses and positive definite SPH kernels W is guaranteed to deliver a positive density estimate. One could, however, also integrate ρ^* forward in time as an alternative. Our computing frame density ρ^* is related to the local rest frame density ρ via

$$\rho^* = \sqrt{-g} \Theta \rho, \quad (9)$$

where Θ is the generalized Lorentz factor

$$\Theta = \frac{1}{\sqrt{-g_{\mu\nu} v^\mu v^\nu}} \quad (10)$$

expressed in terms of the coordinate velocities $v^\mu = dx^\mu/dt$. Note also that, for simplicity, we here use the same symbols S and e as in previous work, although now they have different units. To be able to robustly treat shocks, one has to add dissipative terms. This is done as described in Sec. 2.1.1 of [63].

B. Constraint damping

To harvest the full scientific potential of the next generation of gravitational wave detectors, numerical relativity simulations need to become more accurate [75, 76].

One obvious way forward is increased numerical resolution, the other is to improve the methods so that at the same resolution higher accuracy can be achieved. In the spirit of the second approach, we improve our spacetime evolution in `SPHINCS_BSSN`, by closely following the suggestions made by Etienne [67] in the Eulerian context. The first change is a modification to the strength of the Kreiss-Oliger (KO) [77] dissipation for various variables in different regions. The idea is that dissipation should be decreased where the curvature is large, since we do not want to flatten out large gradients in the fields and dissipation should be increased for the gauge variables, since we want to smooth out sharp features as much as possible. It is convenient to use the conformal factor ϕ as a measure of the curvature and the strength of the dissipation then becomes dependent on ϕ as

$$\epsilon_{\text{KO}}(\phi) = \epsilon_{\text{KO,CA}} e^{-2\phi}, \quad (11)$$

where $\epsilon_{\text{KO,CA}}$ is 0.99 for gauge variables and 0.2 for all other BSSN variables. This modification is expected to be less important for binary neutron stars compared to binary black hole systems as the curvature is smaller, and features in the gauges are expected to be less sharp.

The second improvement is the addition of constraint damping, and therefore involves the Hamiltonian constraint, which in terms of BSSN variables can be written as

$$\mathcal{H} = \frac{2}{3} K^2 - \tilde{A}_{ij} \tilde{A}^{ij} + e^{-4\phi} (\tilde{R} - 8\tilde{D}^i \phi \tilde{D}_i \phi - 8\tilde{D}^2 \phi) = 0. \quad (12)$$

The needed change is an additional term to the RHS equation for the conformal factor ϕ , i.e.

$$\partial_t \phi = [\partial_t \phi]_{\text{STD}} - \kappa_{\phi \mathcal{H}} \mathcal{H}, \quad (13)$$

where $\kappa_{\phi \mathcal{H}}$ has to be chosen small enough to maintain stability. As the constraints contain second derivatives of the field variables, this essentially adds a parabolic term to the evolution equation for ϕ . This introduces a Courant stability requirement, see e.g. [78], such that the timestep Δt scales as Δs_n^2 , where Δs_n is the spatial resolution on refinement level n . That means that $\kappa_{\phi \mathcal{H}}$ has to be small where the resolution is high, but can be increased significantly where the resolution is low. Since we are taking the same timestep on all refinement levels, we choose to scale $\kappa_{\phi \mathcal{H}}$ as

$$\kappa_{\phi \mathcal{H}} = C \frac{\Delta s_n^2}{\Delta t}. \quad (14)$$

In [67] it was reported, based on many experiments in a Eulerian context, that the value $C = 0.15$ leads to stable evolutions. We have found problems in some simulations when using this value of C , so we decrease this value slightly to $C = 0.14$, which has worked well in all cases so far.

C. Thermal equation of state

Much of the merger dynamics and final outcome (e.g. whether/when a BH forms) – as well as the observable signatures (GWs, neutrinos and ejecta/electromagnetic emission) – crucially depend on the (not so well known) nuclear matter equation of state (EOS). The simplest approximation is a polytropic EOS with a single polytropic exponent Γ . A significantly better approach is to use piecewise polytropic EOSs whose polytropic pieces have been fitted to cold nuclear matter EOSs, e.g. [79]. Such approaches are often enhanced by an ideal gas law type thermal EOSs that approximate thermal effects with a thermal exponent Γ_{th} .

Clearly better, however, are EOSs that are based on the state-of-the-art microscopic calculations. Such calculations are way to expensive to be performed “on the fly” during a dynamical merger simulation. Therefore, the most common approach is to interpolate between values in pre-computed tables, provided for example via the COMPOSE database [80]. The use of tabulated EOS requires non-trivial algorithms to recover the physical (“primitive”) variables (e.g. v^i, P, u) from the numerical (“conservative”) ones (ρ^*, S_i, e , see Sec. II A) and we are also following such an approach within SPHINCS_BSSN [81]. Once the “con-to-prim” algorithm is working robustly, it is straight forward to explore new EOS-physics: one only needs to replace one table by another.

But there are also shortcomings related to tabulated equations of state. First, the “con-to-prim” recovery usually requires many table interpolation calls that come at a high computational burden. Moreover, such tables can be non-smooth which may require many iterations to convergence, and, in the worst case, one may even fail to find the correct physical solution. In such cases one may still try to find a solution by means of a more robust, but usually slower fallback-algorithm. Second, the tables are usually restricted to temperatures above ~ 0.1 MeV and to densities above $\sim 10^3$ gcm $^{-3}$. If the focus of a study are the ejecta of a merger, these limits may become detrimental, since the ejecta very quickly run outside of the table boundaries and one has to resort to fallback strategies such as calculating pressures etc. from the (too high) table boundaries, blending the EOS with another, lower-density EOS or even extrapolating, none of which is an ideal option.

We adopt here the finite-temperature extension introduced by Raithel et al. [70], which provides a physically motivated and analytic prescription for augmenting cold equations of state with thermal effects. In the following, we summarize the main elements of this framework and describe our implementation in SPHINCS_BSSN.

1. Finite-temperature EOS framework

Following Ref. [70], the energy per particle of nuclear matter is expanded as a Taylor series in the neutron ex-

cess parameter $(1 - 2Y_p)$ up to second order:

$$E_{\text{nuc}}(n, Y_p, T) = E_{\text{nuc}}(n, Y_p = 1/2, T) + E_{\text{sym}}(n, T)(1 - 2Y_p)^2 \quad (15)$$

Here, $E_{\text{nuc}}(n, Y_p = 1/2, T)$ represents the energy of symmetric nuclear matter. The symmetry energy is defined as

$$E_{\text{sym}}(n, T) = \frac{1}{2} \frac{\partial^2 E_{\text{nuc}}(n, Y_p, T)}{\partial(1 - 2Y_p)^2} \Big|_{Y_p=1/2}. \quad (16)$$

To satisfy charge neutrality, we set the proton and electron densities equal, leading to

$$n_e = Y_p n. \quad (17)$$

Expanding Eq. (15), the energy of symmetric nuclear matter can be expressed as the sum of the cold symmetric matter energy and the thermal contribution:

$$\begin{aligned} E_{\text{nuc}}(n, Y_p, T) &= E_{\text{nuc}}(n, Y_p = 1/2, T = 0) \\ &+ E_{\text{nuc,th}}(n, Y_p = 1/2, T) \\ &+ E_{\text{sym}}(n, T)(1 - 2Y_p)^2. \end{aligned} \quad (18)$$

Since the model is based on a cold EOS in β -equilibrium, this should be reflected in the energy per particle. To achieve this, we eliminate the cold symmetric term as,

$$\begin{aligned} E_{\text{nuc}}(n, Y_p, T) &= E_{\text{nuc}}(n, Y_{p,\beta}, T = 0) + E_{\text{nuc,th}}(n, 1/2, T) \\ &+ E_{\text{sym}}(n, T)(1 - 2Y_p)^2 \\ &- E_{\text{sym}}(n, T = 0)(1 - 2Y_{p,\beta})^2. \end{aligned} \quad (19)$$

Here, $Y_{p,\beta}$ denotes the proton fraction at zero temperature in β -equilibrium.

The final step in completing this generalized model is to incorporate the contributions of leptons and photons into the system. These contributions can also be written as the sum of a cold and a thermal part. In the zero-temperature limit, the energy contribution from relativistic degenerate electrons is given by

$$E_{\text{lepton}}(n, Y_p, T = 0) = 3KY_p(Y_p n)^{1/3}, \quad (20)$$

where

$$K \equiv \frac{(3\pi^2)^{1/3}}{4} \hbar c. \quad (21)$$

The total energy is given by:

$$\begin{aligned} E(n, Y_p, T) &= E(n, Y_p, T = 0) + E_{\text{th}}(n, Y_p, T), \\ E(n, Y_p, T = 0) &= E(n, Y_{p,\beta}, T = 0) + E_{\text{sym}}(n, T = 0) \\ &\times [(1 - 2Y_p)^2 - (1 - 2Y_{p,\beta})^2] \\ &+ 3K \left(Y_p^{4/3} - Y_{p,\beta}^{4/3} \right) n^{1/3}, \\ E_{\text{th}}(n, Y_p, T) &= E_{\text{nuc,th}}(n, 1/2, T) \\ &+ E_{\text{lepton, th}}(n, Y_p, T) \\ &+ E_{\text{sym}}(n, T)(1 - 2Y_p)^2 \end{aligned} \quad (22)$$

2. Symmetry energy at zero temperature

The symmetry-energy parameterization adopted here follows exactly the prescription of Li et al. [82] as implemented in Ref. [70],

$$E_{\text{sym}}(n, T = 0) = \eta E_{\text{sym}}^{\text{kin}}(n) + [S_0 - \eta E_{\text{sym}}^{\text{kin}}(n_{\text{sat}})] \left(\frac{n}{n_{\text{sat}}} \right)^\gamma. \quad (23)$$

Here, $E_{\text{kin}}(n)$ represents the kinetic part of the symmetry energy, while the second term corresponds to the potential part. Since the expression for the potential symmetry energy is not well-constrained by experiments, it is written as the difference between the symmetry energy at saturation density, $S_0 \equiv E_{\text{sym}}(n_{\text{sat}})$, and the kinetic part. A density dependence is introduced through the parameter γ , which controls the rate of change of the symmetry energy due to short-range correlations. Finally, the parameter η is introduced to account for short-range interactions between proton-neutron pairs.

The kinetic symmetry energy can be expressed in terms of the momentum distribution. The kinetic energy per particle, $\varepsilon_{k,q}$, is given by

$$\varepsilon_{k,q} = 3E_f(n_q)n^{5/3},$$

where q represents the particle (either a neutron or proton) and $E_f(n)$ is the Fermi energy

$$E_f(n_q) = \frac{\hbar^2}{2m} (3\pi^2 n_q)^{2/3},$$

with m representing the mass of the particle. The small difference between the proton and neutron masses is neglected, so we approximate $m \approx m_n$, where m_n is the neutron mass.

Since the kinetic symmetry energy arises due to the change in the Fermi energy of a gas as the proton fraction varies between symmetric matter and neutron matter, it can be expressed as a function of the total baryon density n as

$$\begin{aligned} E_{\text{sym}}^{\text{kin}}(n) &= \frac{3}{5} \left[2E_f \left(n_p = n_n = \frac{1}{2}n \right) - E_f(n_n = n) \right] \\ &= \frac{3}{5} (2^{1/3} - 1) E_f(n), \end{aligned} \quad (24)$$

where $E_f(n)$ represents the Fermi energy as a function of total density.

An expression for the symmetry energy at zero temperature can be derived, see e.g. [83, 84], which depends on three parameters: S_0 , L , and γ , all of which are experimentally constrained. The remaining task is to establish a relationship between the symmetry energy at zero temperature and the proton fraction for matter in beta-equilibrium, $Y_{p,\beta}$, which is the primary result extracted

from our data. This relationship is given by

$$Y_{p,\beta} = \frac{1}{2} + \frac{(2\pi^2)^{1/3}}{32} \frac{n}{\xi} \left\{ (2\pi^2)^{1/3} - \frac{\xi^2}{n} \left[\frac{\hbar c}{E_{\text{sym}}(n, T = 0)} \right]^3 \right\}, \quad (25)$$

where, for convenience, one introduces the auxiliary quantity ξ , defined as

$$\xi \equiv \left[\frac{E_{\text{sym}}(n, T = 0)}{\hbar c} \right]^2 \times \left\{ 24n \left[1 + \sqrt{1 + \frac{\pi^2 n}{288} \left(\frac{\hbar c}{E_{\text{sym}}(n, T = 0)} \right)^3} \right] \right\}^{1/3}. \quad (26)$$

At densities below $0.5 n_s$, nuclei begin to form, and the expansion formalism for the nuclear symmetry energy breaks down. To handle this transition, we require a reasonable extrapolation of the symmetry energy model to integrate with a known low-density EoS table. Following Ref. [85], we empirically choose a power-law decay model for the symmetry energy extrapolation to ensure that E_{sym} (1) remains positive and real, (2) diminishes its contribution to the overall energy, and (3) predicts $Y_{e,\beta} \in (0, 0.5]$, with $Y_{e,\beta}$ approaching the value from SFHo at low densities. For $n < 0.5 n_s$, we adopt the following model for the symmetry energy:

$$E_{\text{sym,low}}(n) = [1 - \chi(n)]E_{\text{fl}} + \chi(n)E_{\text{PL}}(n), \quad (27)$$

where $E_{\text{PL}}(n)$ represents a power-law function and E_{fl} is an energy floor, set to 11.22 MeV. This floor corresponds to $E_{\text{sym}}(0.5 n_s)/2$, calculated using the best-fit parameters for the SFHo EoS [86] ($S = 31.47$ MeV, $L = 47.10$ MeV, $\gamma = 0.41$; [70]). In this expression, $\chi(n)$ is a smooth transition function given by

$$\chi(n) = \frac{1 + \tanh[X(n - n_0)]}{2}, \quad (28)$$

where we select $X = 40$ and $n_0 = 0.025$ fm $^{-3}$, ensuring that $\chi(n) \approx 1$ at $0.5 n_s$ (to within 1% accuracy) and $\chi(n)$ decreases at lower densities. These parameters and the value of E_{fl} were chosen empirically to ensure that $Y_{p,\beta}(n)$ closely matches that of SFHo in this density range for the EoSs considered in this work.

To ensure continuity in the symmetry energy and corresponding pressure, we define the power-law energy extrapolation as

$$E_{\text{PL}}(n) = E_{\text{sym}}(n_t) + \frac{P_{\text{sym}}(n_t)}{n_t(\gamma_{\text{PL}} - 1)} \left[\left(\frac{n}{n_t} \right)^{\gamma_{\text{PL}} - 1} - 1 \right], \quad (29)$$

where $n_t = 0.5 n_s$, and the power-law index γ_{PL} is given by

$$\gamma_{\text{PL}} = \frac{\partial P_{\text{sym}}(n)}{\partial n} \bigg|_{n_t} \left[\frac{n_t}{P_{\text{sym}}(n_t)} \right], \quad (30)$$

and $P_{\text{sym}}(n) = n^2 \frac{\partial E_{\text{sym}}(n)}{\partial n}$. For the corresponding model of the low-density symmetry pressure, we neglect the density derivatives of $\chi(n)$, as they introduce unphysical density dependencies. Instead, we calculate the pressure in the two asymptotic limits and use $\chi(n)$ to smoothly connect these regions:

$$\begin{aligned} P_{\text{sym,low}}(n) &= n^2 \left(\frac{\partial E_{\text{fl}}}{\partial n} \right) [1 - \chi(n)] + n^2 \left(\frac{\partial E_{\text{PL}}(n)}{\partial n} \right) \chi(n) \\ &= P_{\text{PL}}(n) \chi(n), \end{aligned} \quad (31)$$

where the first term vanishes since E_{fl} is constant, leaving the expression:

$$P_{\text{PL}}(n) = P_{\text{sym}}(n_t) \left(\frac{n}{n_t} \right)^{\gamma_{\text{PL}}}. \quad (32)$$

3. Thermal contribution to the energy

To describe the thermal contribution to the energy per baryon in npe -matter, we define, following [70], the thermal energy as a piecewise function that accounts for relativistic, ideal-fluid, and degenerate regimes. This allows capturing the dominant thermal physics across density ranges of astrophysical interest.

It is, therefore, convenient to express the thermal energy per particle as

$$E_{\text{th}}(n, Y_p, T) = \begin{cases} E_{\text{rel}}(n, T), & n < n_1, \\ E_{\text{ideal}}(T), & n_1 < n < n_2, \\ E_{\text{th,deg}}(n, Y_p = \frac{1}{2}, T) \\ + E_{\text{sym,th}}(n, T)(1 - 2Y_p)^2, & n > n_2, \end{cases} \quad (33)$$

where:

$$E_{\text{rel}}(n, T) = \frac{4\sigma f_s T^4}{cn}, \quad (34)$$

$$E_{\text{ideal}}(T) = \frac{3}{2} k_B T. \quad (35)$$

Here, $E_{\text{th,deg}}(n, Y_p = 1/2, T)$ is the degenerate thermal energy in symmetric matter, introduced below. Because the relativistic and ideal-fluid components do not depend on the proton fraction Y_p , the symmetry-energy correction appears only in the degenerate regime.

The transition densities n_1 and n_2 are defined as the densities at which the relativistic and ideal-fluid thermal energies are equal, and where the ideal-fluid and degenerate thermal energies are equal, respectively. These densities depend on both temperature and composition.

Degenerate Thermal Energy

In the degenerate regime, we model nucleons as a free Fermi gas. The leading-order thermal energy per baryon for a species q is

$$E_{\text{th, q}}^{\text{deg}}(n, Y_q, T) = a(Y_q n, M^*) Y_q T^2, \quad (36)$$

where the level-density parameter is

$$a(n_q, M^*) = \frac{\pi^2 k_B^2}{2} \frac{\sqrt{(3\pi^2 n_q)^{2/3} (\hbar c)^2 + M^*(n_q)^2}}{(3\pi^2 n_q)^{2/3} (\hbar c)^2}, \quad (37)$$

and $M^*(n_q)$ is the Dirac effective mass. For a full derivation including next-to-leading order corrections, see Constantinou *et al.* [87].

For symmetric matter, where $n_n = n_p = n/2$, the degenerate thermal energy becomes

$$E_{\text{th, nucl}}^{\text{deg}}(n, T) = a(0.5n, M_{\text{SM}}^*) T^2, \quad (38)$$

assuming $M_{\text{n,SM}}^* \approx M_{\text{p,SM}}^* \approx M_{\text{SM}}^*$.

Leptonic Contribution

For degenerate leptons, particularly electrons, the thermal energy is simpler. Their effective mass remains approximately constant ($M_e^* \approx m_e$). The degenerate electron thermal energy is

$$E_{\text{th, e-}}^{\text{deg}}(n, Y_p, T) = a(Y_p n, m_e) Y_p T^2, \quad (39)$$

where we impose charge neutrality ($Y_e = Y_p$). In the presence of positrons, this should be generalized to the net lepton fraction.

While the above piecewise form is physically motivated and convenient for analytic expressions, the discontinuities at the transition densities can be problematic for numerical simulations. Discontinuities may lead to unphysical reflections of matter waves at interfaces. Therefore, for practical implementations we use a smooth approximation:

$$\begin{aligned} E_{\text{th}}(n, Y_p, T) &\approx E_{\text{rel}}(n, T) + \\ &\quad [E_{\text{ideal}}(T)^{-1} + E_{\text{th,deg}}(n, Y_p, T)^{-1}]^{-1}, \end{aligned} \quad (40)$$

where the inverse sum ensures that E_{ideal} dominates at intermediate densities and $E_{\text{th,deg}}$ dominates at high densities. This smoothed form is also computationally efficient and avoids the explicit calculation of n_1 and n_2 .

With this, the complete energy density equation is given by

$$\begin{aligned} E(n, Y_p, T) &= \underbrace{\left(\text{Cold EOS in } \beta\text{-equilibrium} \right)}_{\text{background}} \\ &\quad + 3K \left(Y_p^{4/3} - Y_{p,\beta}^{4/3} \right) n^{1/3} \\ &\quad + E_{\text{sym}}(n, 0) [(1 - 2Y_p)^2 - (1 - 2Y_{p,\beta})^2] \\ &\quad + E_{\text{th}}(n, Y_p, T). \end{aligned} \quad (41)$$

4. Approximating the Dirac effective mass

With the complete set of equations for the thermal energy available, it becomes clear that calculating this

thermal energy requires knowledge of the Dirac effective masses in symmetric matter. Determining these masses, in turn, depends on understanding the scalar meson interactions and particle potentials for each equation of state. Since such details go beyond the scope of creating a straightforward, physically motivated framework, an approximation for the Dirac effective mass is introduced. This approximation must be consistent with existing data, and thus, it must satisfy two limits: at low densities, the effective mass should approach the dominant nucleon mass, and at high densities, M^* should decrease due to the increased significance of particle interactions. This behavior is captured using the following power-law expression:

$$M^*(n_q) = \left\{ (mc^2)^{-b} + \left[mc^2 \left(\frac{n_q}{n_0} \right)^{-\alpha} \right]^{-b} \right\}^{-1/b}, \quad (42)$$

where m represents the dominant nucleon mass (taken as the neutron mass $mc^2 = 939.57$ MeV), and n_0 is the density above which M^* begins to decrease. The exponent b , which controls the steepness of the transition to the region where the effective mass decreases, is fixed at $b = 2$. Lastly, α is the parameter that defines the slope at high densities. With b fixed, the effective mass is characterized by two free parameters: n_0 and α .

5. The complete pressure equations

Using the energy relations from the previous subsection, the expression for the pressure can be obtained. The pressure for n - p - e matter is given by

$$\begin{aligned} P(n, Y_p, T) = & P_{\text{cold}}(n, Y_p, \beta) + K \left(Y_p^{4/3} - Y_{p,\beta}^{4/3} \right) n^{4/3} \\ & + P_{\text{sym}}(n, T = 0) [(1 - 2Y_p)^2 - (1 - 2Y_{p,\beta})^2] \\ & + P_{\text{th}}(n, Y_p, T). \end{aligned} \quad (43)$$

where the thermal pressure contribution is given by

$$P_{\text{th}}(n, Y_p, T) = \begin{cases} \frac{4\sigma_{\text{fs}} T^4}{3c}, & n < n_1, \\ nk_B T, & n_1 < n < n_2, \\ -\frac{\partial a(0.5n, M_{\text{SM}})}{\partial n} + \frac{\partial a(Y_p n, m_e)}{\partial n} Y_p n^2 T^2, & n > n_2. \end{cases} \quad (44)$$

Here, n_1 and n_2 are the transition densities for thermal pressure at a given temperature and proton fraction. The symmetry pressure is expressed as

$$P_{\text{sym}}(n, T = 0) = \frac{2\eta}{3} n E_{\text{sym}}^{\text{kin}}(n) \quad (45)$$

$$+ \gamma n [S_0 - \eta E_{\text{sym}}^{\text{kin}}(n_{\text{sat}})] \left(\frac{n}{n_{\text{sat}}} \right)^\gamma. \quad (46)$$

As before, we avoid the piecewise expressions for the thermal pressure by using the smooth approximation

$$P_{\text{th}}(n, Y_p, T) \approx P_{\text{rel}} + \left(P_{\text{ideal}}^{-1} + P_{\text{deg}}^{-1} \right)^{-1}. \quad (47)$$

6. The complete entropy equations

The *entropy density* $s(n, n_p, n_n, n_e, T)$, accounting for relativistic, ideal-fluid, and degenerate regimes, is given by

$$s(n, n_p, n_n, n_e, T) = \begin{cases} s_{\text{rel}}, & n < n_1 \\ s_{\text{ideal}}, & n_1 < n < n_2 \\ s_{\text{deg}}, & n > n_2, \end{cases} \quad (48)$$

where n_1 and n_2 are the transition densities for thermal energy.

The entropy density of a gas of relativistic leptons and photons is

$$s_{\text{rel}} = \frac{16\sigma f_s}{3c} (n_p + n_n) T^3. \quad (49)$$

The entropy density of a monatomic ideal fluid is given by the Sackur-Tetrode equation:

$$\begin{aligned} s_{\text{ideal}} = & (n_p + n_n + n_e) k_B \\ & \times \left\{ \ln \left[\left(\frac{n_p + n_n}{n_p + n_n + n_e} \right) n^{-1} \left(\frac{mk_B T}{2\pi\hbar^2} \right)^{3/2} \right] + \frac{5}{2} \right\}. \end{aligned} \quad (50)$$

In the degenerate regime, the entropy density of a Fermi gas of particle species q is

$$s_q = 2a_q n_q T, \quad (51)$$

so that the total degenerate entropy density becomes

$$s_{\text{deg}} = 2 \{ a(0.5n, M_{\text{SM}}^*) (n_p + n_n) + a(Y_p n, m_e) n_e \} T. \quad (52)$$

To provide a continuous interpolation across the relativistic, ideal, and degenerate regimes, we adopt, once more, a smooth approximation

$$s(n, Y_p, T) \approx s_{\text{rel}} + \left(s_{\text{ideal}}^{-1} + s_{\text{deg}}^{-1} \right)^{-1}. \quad (53)$$

7. Numerical implementation

In Appendix A of [63] we outlined in detail how we recover the physical variables from the conserved variables for the case where the cold part of the EOS is given by a piecewise-polytropic representation [88] and the thermal part is given by an ideal gas-type law with a fixed thermal exponent Γ_{th} . Starting from this algorithm, we change

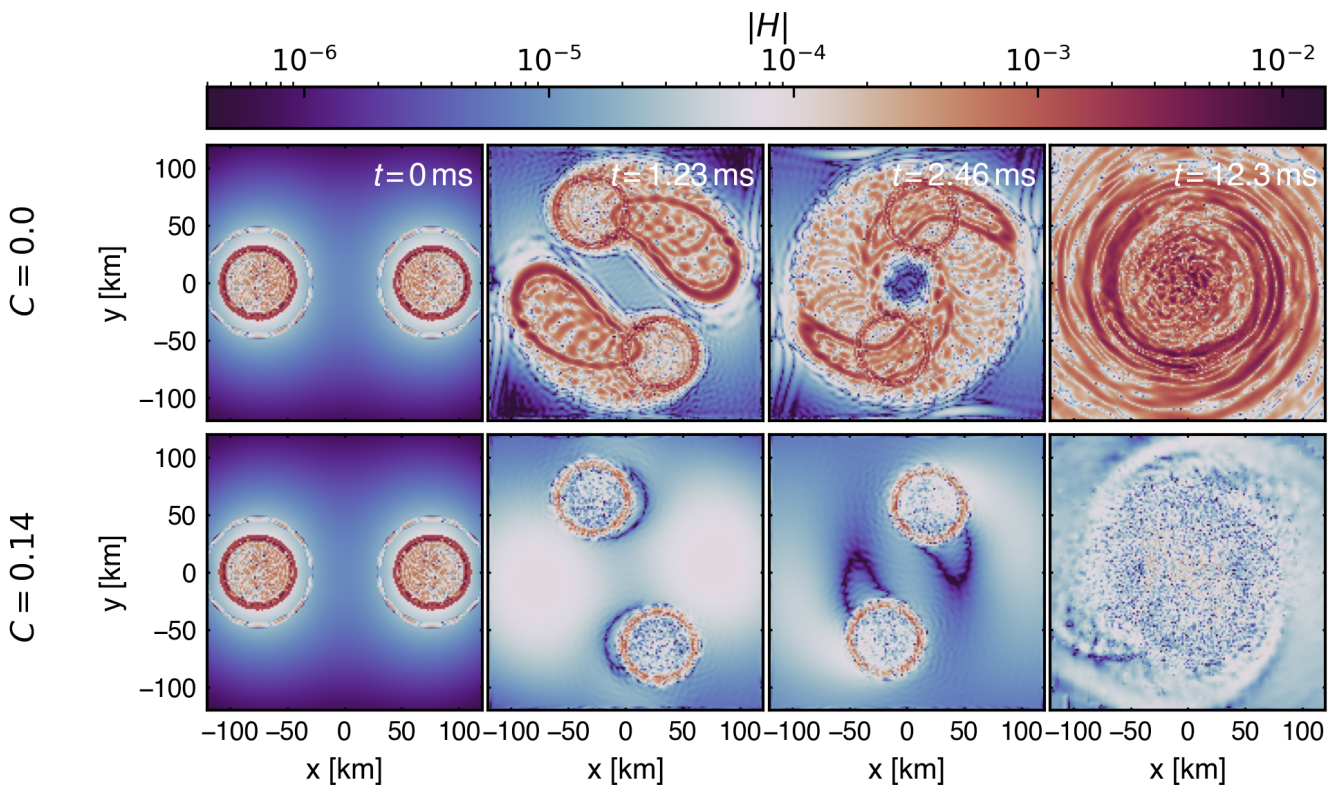


FIG. 1. A comparison of the absolute value of the Hamiltonian constraint in the xy -plane at different times for the 1 million particle runs with no constraint damping (row 1) with the corresponding run with constraint damping (row 2). The first column is for the initial time $T = 0$ ms, the second column is for $T = 1.23$ ms, the third column is for $T = 2.46$ ms and the fourth column is for $T = 12.3$ ms.

the thermal parts to the finite-temperature extension described above. Starting from an initial guess for the pressure, we compute the specific internal energy, separate the cold and thermal components, determine the temperature from the thermal model, and update the thermal pressure accordingly. The pressure is then corrected until the cold and thermal contributions self-consistently match the evolved state. Both the pressure and temperature inversions are solved using *Ridders' root-finding method* [89, 90], which is a powerful variant of the *regula falsi*. This method has a number of desirable properties, for example, it does not need derivatives, it does not jump out of the brackets, is generally very robust and it converges fast.

III. RESULTS

We demonstrate here the new elements in SPHINCS_BSSN. In all cases we use the ENG EOS [91] which is consistent with known constraints on the neutron star equation of state [92]. Each simulation is performed for an equal-mass binary with component masses of either $1.3 M_{\odot}$ or $1.4 M_{\odot}$, starting from quasi-circular orbits at an initial coordinate separation

of 45 km, where the initial data were constructed using the FUKA [93] library and the code SPHINCS_ID [61, 64] was used for the particle placement.

We first demonstrate the effect of the constraint damping terms, see Sec. III A, then we discuss thermal effects in a merger, see Sec. III B, and whether it is likely to determine the involved parameters from potential post-merger observations with future GW-facilities. We finally summarize our results in Sec. IV.

A. Effect of Constraint Damping

To illustrate the effect of the constraint damping we performed simulations with one and two million SPH particles for a baseline setup ($2 \times 1.3 M_{\odot}$, ENG equation of state), both without ($C = 0$) and with ($C = 0.14$) constraint damping turned on, where C refers to the strength of the constraint damping as defined in Eq. (14). In Fig. 1, we show a comparison of the absolute value of the Hamiltonian constraint violation in the orbital plane for runs without constraint damping (row 1) and with constraint damping (row 2) at times $t = 0$ ms (column 1), $t = 1.23$ ms (column 2), $t = 2.46$ ms (column 3) and $t = 12.3$ ms (column 4). For both runs, it is clear

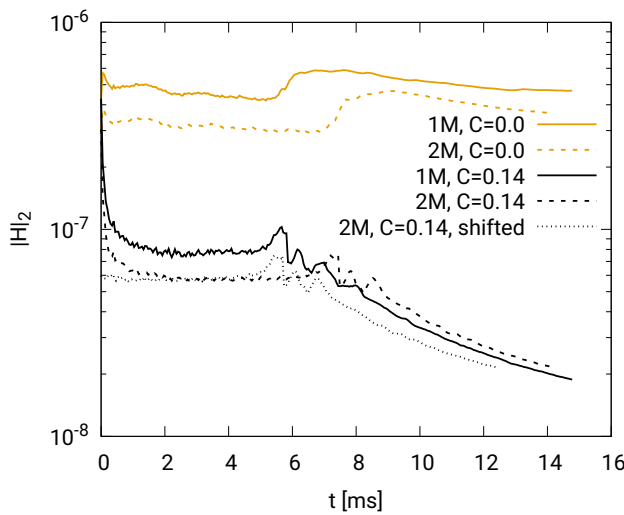


FIG. 2. The L^2 -norm of the Hamiltonian constraint as function of time. In this plot no constraint damping is shown with the orange curves, while full constraint damping is shown with the black curves. Runs with one million particles are shown with solid curves, while two million particles are shown with dashed curves. Finally the dotted line shows the two million particle run with constraint damping shifted in time so that the merger time is aligned with the one-million-particle run.

that the constraint violations are mostly triggered by the sharp surfaces of the stars. The main difference is that in the undamped case the constraint violations persist, due to the zero speed constraint mode in the BSSN equations, when the stars move away, leaving a significant trail of constraint violations, whereas the constraint violations are clearly damped behind the stars when the damping is turned on. So, without constraint damping, the whole interior of the orbit is eventually filled with constraint violations. After the merger, there is no longer a sharp surface, as low density material surrounds the merger remnant. At late times after the merger, the constraint violations are significantly reduced in the constraint damped case compared to the undamped case. Since we are using a global timestep, we can increase the strength of the constraint damping on the coarser grids (for every factor of 2 in resolution, we can increase the strength by a factor of 4).

In Fig. 2 we show the L^2 norm of the Hamiltonian constraint as a function of time. In this plot the orange curves are for runs without constraint damping ($C = 0$) while black curves are for runs with constraint damping ($C = 0.14$), solid curves are for runs with one million particles, dashed curves are for two million particles, and the dotted line is for the constraint damped run with two million particles shifted in time to align the merger time with the one million particle run.

In the undamped case, the L^2 norm of the constraint violations grows rapidly initially, then stays roughly constant during the inspiral phase, grows again during the merger, and then only decreases slightly after the merger.

In the damped case, on the other hand, the constraint violations drop rapidly from the initial value, then stay roughly constant during the inspiral (at a level about 5 to 6 times lower than the undamped case), increase slightly during the merger, but with the disappearance of the sharp neutron star surfaces, continues to decrease significantly, so that at the end they are about 20 times smaller than in the undamped case. The dotted curve (shifting the two million particle constraint damped case in time to align the merger with the one million particle case), have been added to make it clear that the constraint violations decrease with resolution.

B. Effect of Thermal Equation of State

We will first discuss the temperature evolution of generic neutron star merger ($2 \times 1.4 M_\odot$, no initial spins, ENG equation of state), and then we systematically explore the impact of the Dirac effective mass parameters n_0 and α in the thermal EOS. We also monitor the impact on ejecta and we explore the imprint on the resulting post-merger GW-signal.

1. Illustrative case

We first focus on a generic neutron star merger of two $1.4 M_\odot$ neutron stars with the ENG-EOS and a fiducial set of parameters for the Dirac mass M^* , $n_0 = 0.1$, $\alpha = 0.9$ in Eq. (42). During the inspiral the temperatures remain at essentially zero. The particles only reach temperatures of ~ 1 MeV in the surface layers, within the outermost few hundred meters, where the densities drop by orders of magnitude and the particles have to continuously adjust to the dynamically changing tides, see Fig. 3. This temperature is about an order on magnitude lower than what is typically found in Eulerian numerical relativity simulations, see e.g. [94, 95]. During the merger the shear layer between the stars is Kelvin-Helmholtz unstable, and peak temperatures exceeding 80 MeV are reached (very locally) in the resulting vortices during the maximum compression phase, approximately corresponding to the snapshot shown in the first column in Fig. 4. The central regions of the remnant undergo several bounces, and thereby heat up the central remnant. Note that for visibility reasons we have restricted the color bar to a maximum of 30 MeV in all of the panels. The hot matter from the interface region is sheared out and spreads around the central remnant, see column 2, and at later times, see column 3, the core is only moderately hot with $T \sim 10$ MeV, but engulfed by hot surface layers of $T \sim 30$ MeV. While the details certainly depend on the astrophysical parameters of the merging binary (masses, mass ratio, spins etc.) and the equation of state used, our results are qualitatively in very good agreement with the results found by other thermal EOS

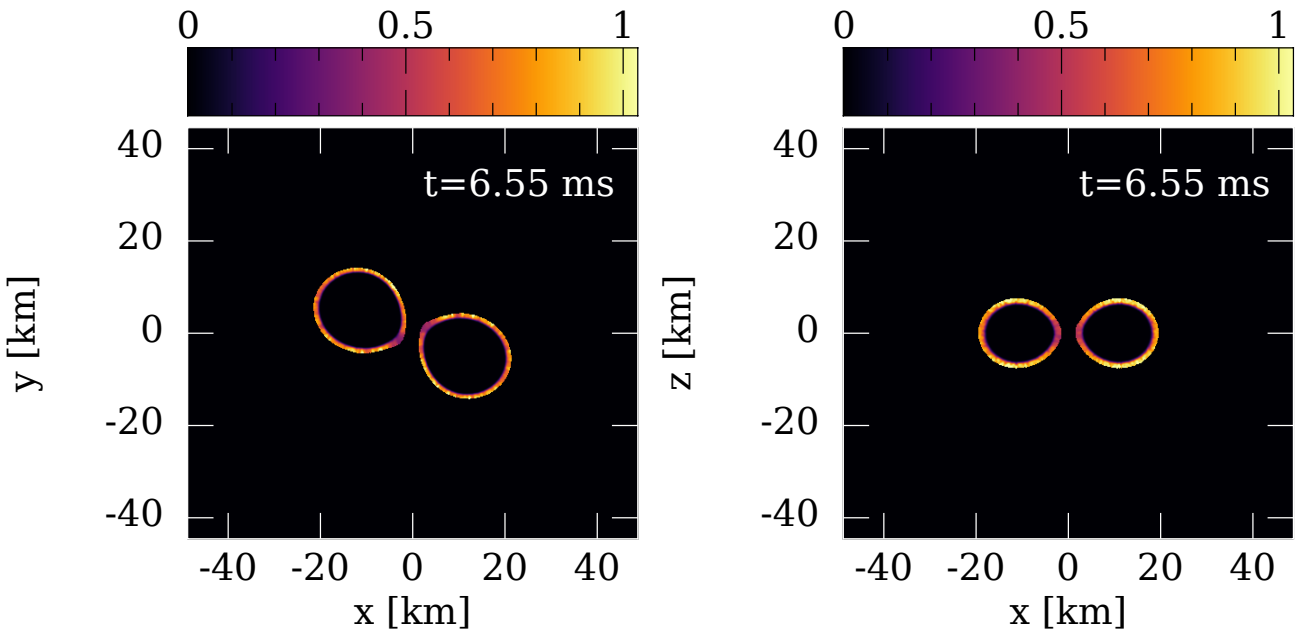


FIG. 3. Temperature distribution (in MeV) the illustrative example ($2 \times 1.4 M_{\odot}$, three million particles; see text for more details) just before the merger.

implementations [70, 71, 96, 97] and with simulations using tabulated EOSs, see e.g. [98].

2. Impact of the Dirac effective mass parameters

To probe uncertainties in the degenerate thermal pressure, we varied the parameters controlling the Dirac effective mass $M^*(n)$, namely n_0 and α in Eq. (42). Specifically, we considered three representative values of n_0 (0.01, 0.12, and 0.40 fm^{-3}) and three values of the slope parameter α (0.2, 0.8, and 1.2). This set brackets the plausible range of thermal responses while keeping the cold EOS fixed [70]. The pressures resulting from these choices are shown as a function of density in Fig. 5 at $T = 1, 10, 20, 30 \text{ MeV}$ and $Y_p = 0.1$. Each of our nine simulations (three n_0 and three α values) was performed for an equal-mass binary with component masses of $1.3 M_{\odot}$, starting from quasi-circular orbits at an initial coordinate separation of 45 km and evolved through merger and $\sim 20 \text{ ms}$ of post-merger evolution.

Density and temperature evolution

The evolution of the minimum lapse function, $\alpha_{\min}(t)$, and the maximum rest-mass density, $\rho_{\max}(t)$, can be seen as proxies for the overall dynamical evolution. In particular, if the remnant should undergo collapse towards a BH, $\rho_{\max}(t)$ would dramatically increase while $\alpha_{\min}(t)$ would drop towards zero. Figure 6 demonstrates that all models follow the same qualitative trend which is characteristic for mergers that leave a stable (or

long-lived) remnant: α_{\min} decreases sharply at merger, reaching a minimum, and then it exhibits damped oscillations as the remnant settles into what seems a stable configuration. Up to late times ($\sim 20 \text{ ms}$) the lapse remains stable across all thermal EOS parameterizations, none of the models indicates any tendency of collapse. The corresponding maximum density evolution, shown in Fig. 7, shows strong oscillations during the first few milliseconds after merger, reflecting the nonlinear core dynamics of the hypermassive remnant. These oscillations gradually damp, and ρ_{\max} approaches a quasi-stationary value without signs of runaway growth. This behavior is consistent with the lapse diagnostics and confirms that the remnant remains supported against collapse for all thermal models considered here. In Fig. 8 we show the peak temperature evolutions found as an average over the 100 hottest SPH particles. During the inspiral, all models remain essentially cold with temperatures below $T \sim 1 \text{ MeV}$. During the first deep compression in the merger, short-lived temperature spikes of $\sim 80\text{--}100 \text{ MeV}$ appear in the contact layers and Kelvin-Helmholtz hotspots, consistent with the illustrative case. The timing and amplitude of these peaks vary across parameter choices, with low- n_0 models reaching their maxima later due to a slightly longer inspiral time. Within the next 1–3 ms, the temperatures settle near $T \sim 30 \text{ MeV}$.

Fig. 9 shows the thermal energies in the high-density regions with $\rho > 10^{14} \text{ g cm}^{-3}$. During the inspiral E_{th} reaches a plateau of a few 10^{48} erg . Differences between the models already appear at this stage, sug-

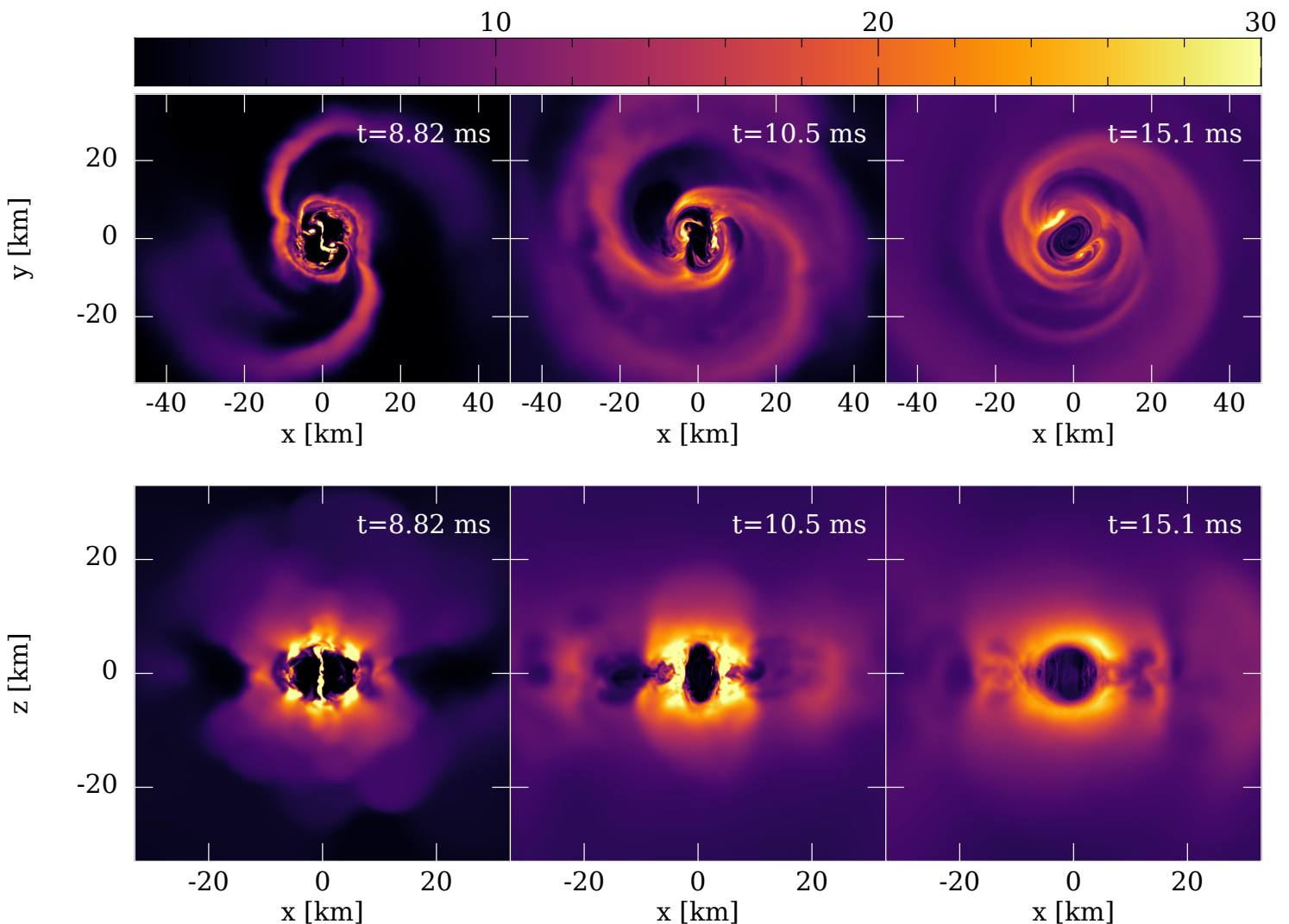


FIG. 4. Temperature distribution (first row: XY -plane, second row: XZ -plane) in a merger of $2 \times 1.4 M_{\odot}$. For visibility reasons the color bar is restricted to values below 30 MeV. Very locally and for a short time (around the time shown in the first panel), peak temperatures exceed 80 MeV.

gesting that variations in the thermal response develop during the inspiral and may influence the subsequent merger. At merger, the thermal energy increases sharply to several 10^{52} erg in all simulations. The strongest and latest rises occur for the low- n_0 models with larger α , consistent with their delayed merger times. After this phase, the high-density thermal energy remains largely constant, in line with the presence of a long-lived remnant and our disregard of neutrino cooling.

Impact of the thermal EOS on the inspiral

As shown in Fig. 3, the neutron star cores remain essentially cold, but the surface temperatures reach values of order ~ 1 MeV, leading to a non-negligible thermal pressure contribution in the outermost layers. The effect is most pronounced for low values of n_0 and larger

values of α (in particular $n_0 = 0.01$ with $\alpha = 0.8$ and 1.2), for which the degenerate-matter thermal pressure at $T = 1$ MeV is noticeably smaller, as seen in the top-left panel of Fig. 5. This reduced thermal support effectively results in slightly more compact stars, smaller tidal effects and a correspondingly delayed merger. The effect is minor for the overall dynamics, but it appears in more than one diagnostic and points to a systematic change in the late-inspiral evolution. To understand its origin, we focus on the two parameterizations that yield the earliest and latest merger, $(n_0, \alpha) = (0.4, 0.2)$ and $(0.01, 1.2)$, respectively. Figure 10 (top) shows a snapshot of the orbital-plane at $t = 6.90$ ms. At this time, the $(0.4, 0.2)$ case is already strongly tidally deformed: the high-density region is visibly stretched along the line connecting the center of masses (COMs) of the two neu-

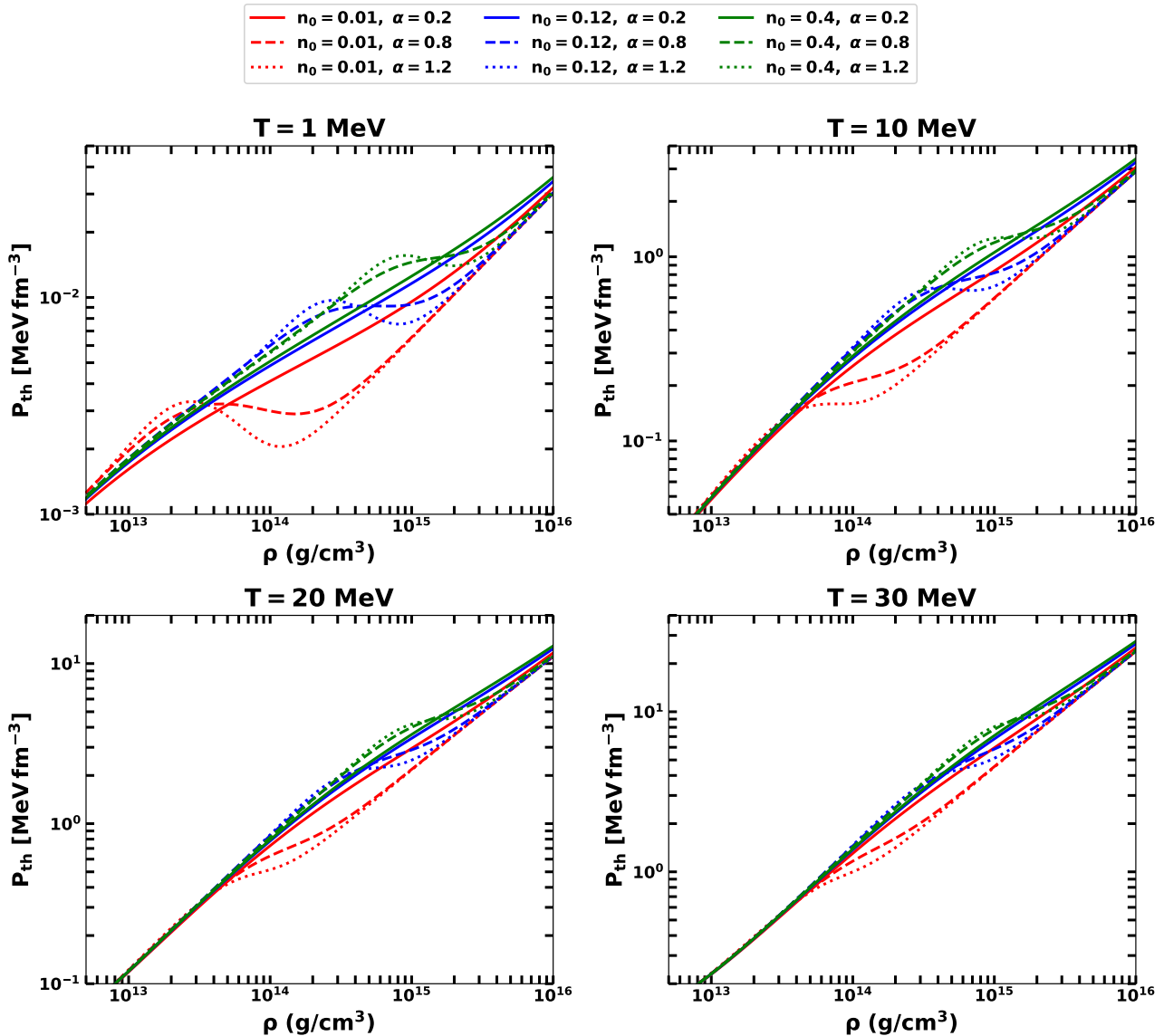


FIG. 5. Thermal pressure P_{th} as a function of density ρ for four temperatures ($T = 1, 10, 20, 30$ MeV) at $Y_e = 0.1$. Note that for visibility reasons the y-axis ranges are different.

tron stars, while the (0.01, 1.2) case remains closer to nearly spherical stars. We quantify this trend by measuring, for each star, its extent along three orthogonal directions: (i) along the line connecting the COMs of the neutron stars, (ii) the direction perpendicular to it within the orbital plane, and (iii) the direction normal to the orbital plane (the z -direction). The elongations L_i are computed from the region with $\rho \geq 10^{11} \text{ g cm}^{-3}$, and we define the dimensionless deformation measure

$$\eta \equiv \frac{L_{\max} - L_{\min}}{L_{\max} + L_{\min}}. \quad (54)$$

The evolution of $\eta(t)$ during inspiral, given in Fig. 10 (bottom), shows that the (0.4, 0.2) run develops a stronger elongation earlier in time. The associated increase in effective radius enhances the tidal interaction

and, given the strong radius dependence of the tidal deformability parameter $\Lambda \sim R^5$ (e.g. Hinderer *et al.* 99), leads to an accelerated inspiral and an earlier merger.

Dynamical ejecta

In Fig. 11 we show the impact of effective mass parameters (n_0, α) on the dynamical ejecta. We find that they have a noticeable effect on the total ejecta mass, with variations of up to a factor of two across the explored range. To determine whether these differences also alter the angular or kinematic structure of the ejecta, we study the mass distribution as a function of polar angle. These profiles show no significant deviations between parameter choices: all models eject most mass toward the orbital plane and exhibit a strong decline toward

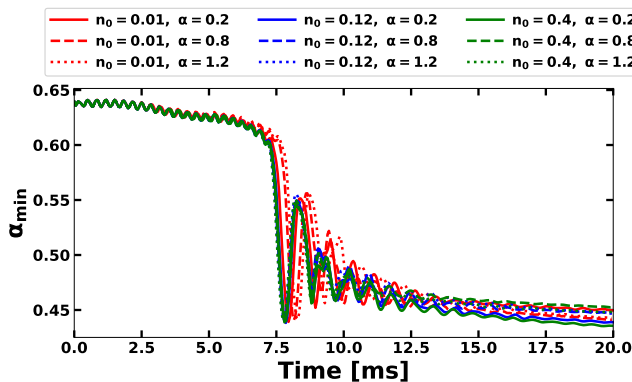


FIG. 6. Time evolution of the minimum lapse $\alpha_{\min}(t)$ for different thermal EOS parameterizations (n_0, α) at 2×10^6 particles. The lapse remains stable at late times, indicating that the remnant does not collapse within the simulated duration for any of the thermal treatments considered here.

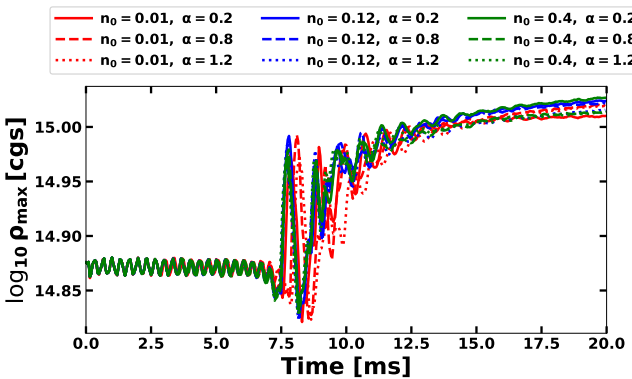


FIG. 7. Time evolution of the maximum rest-mass density $\rho_{\max}(t)$ for different thermal EOS parameterizations (n_0, α) at 2×10^6 particles. Oscillations are clearly seen in the first few milliseconds after merger, but ρ_{\max} remains bounded at late times, confirming that no collapse occurs within the simulation window.

angles close to the polar axis. This funnel near the poles is consistent with the expected geometry of neutron-star mergers. For completeness we also analyze the normalized mass in different velocity bins, $M_{\text{ej,v}}/M_{\text{ej}}^{\text{tot}}$. The histograms in Fig. 12 look nearly identical, indicating that the velocity structure of the dynamical ejecta is largely insensitive to (n_0, α) . Together, these results show that the Dirac-mass parameters mainly rescale the total ejecta mass, while the angular and velocity profiles are governed by the cold EOS part and change little with the thermal response.

GWs and post-merger GW spectrum

Figure 13 shows the plus polarization of the $(2, 2)$ mode of the gravitational-wave strain extracted from simulations with 2×10^6 SPH particles for different parameterizations of the effective mass [cf. Eq. (42)]. During the early in-

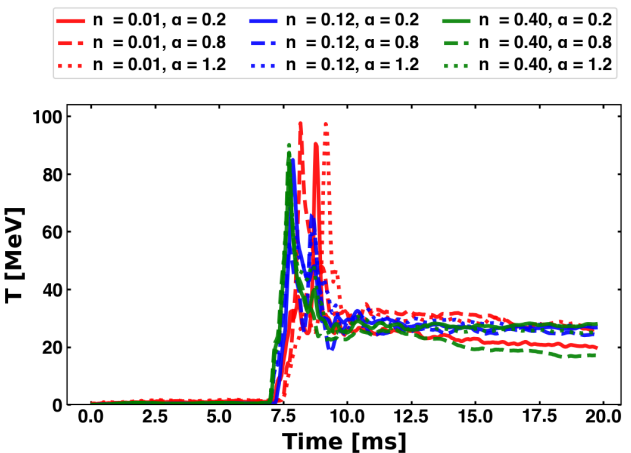


FIG. 8. Average temperature of the 100 hottest SPH particles as a function of time for the explored thermal EOS parameterizations.

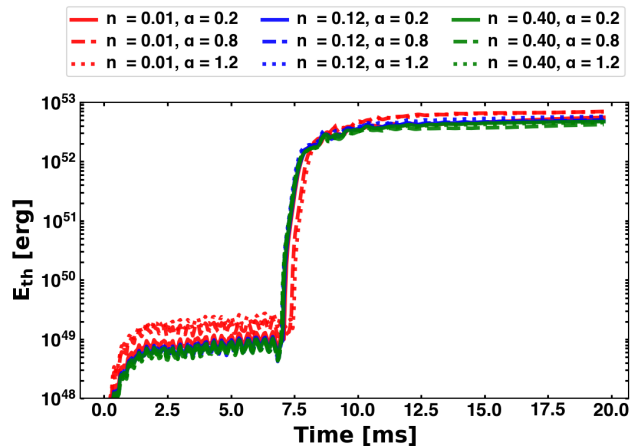


FIG. 9. Integrated thermal energy in the high-density region $\rho > 10^{14} \text{ g cm}^{-3}$ as a function of time for different (n_0, α) choices.

spiral, the waveforms overlap nearly perfectly across all thermal EOS extensions, consistent with the expectation that the bulk inspiral dynamics are governed by the cold EOS. However, in the late inspiral we observe small but systematic differences in the phase evolution and in the merger time between different thermal treatments.

After merger, clear differences emerge in the gravitational-wave signal. The remnant undergoes quasi-periodic oscillations with a rapidly decaying amplitude, and both the phase evolution and damping time depend on the thermal EOS parameters (n_0, α) , while the overall waveform morphology remains robust. The corresponding effective amplitude spectra are shown in Fig. 14, together with the sensitivity curves of Advanced LIGO A+ [100], Einstein telescope (ET) [101], and Cosmic Explorer (CE) [102]. All models exhibit a dominant spectral peak in the 2–4 kHz range, associated with the fundamental quadrupolar oscillation mode of the hypermassive

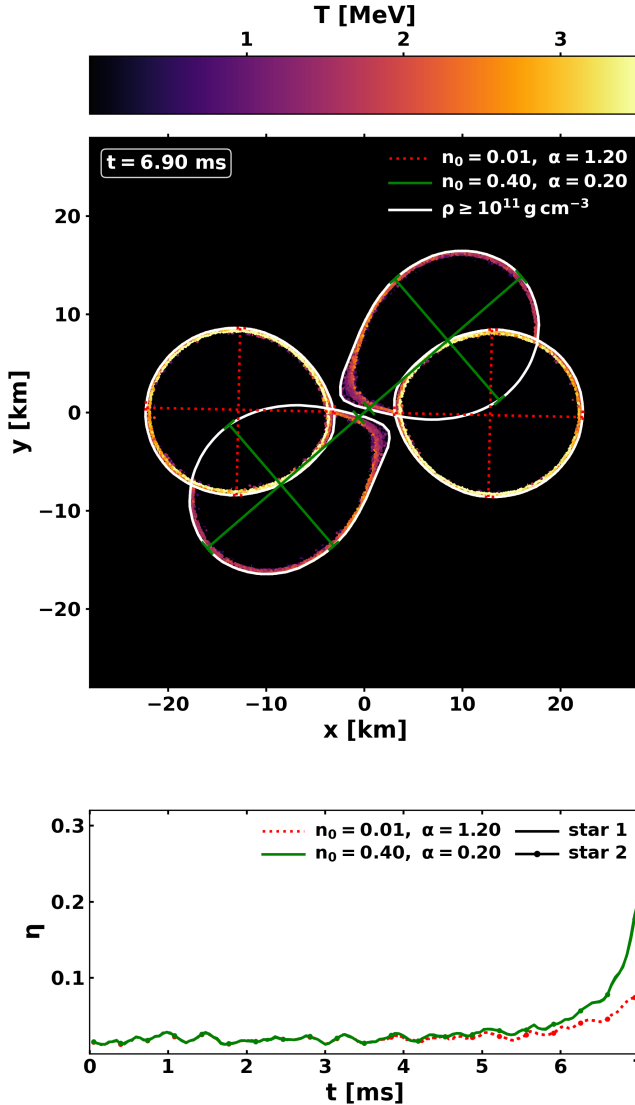


FIG. 10. Tidal deformation in the two simulations with two million particles and the earliest and latest merger times, $(n_0, \alpha) = (0.4, 0.2)$ and $(0.01, 1.2)$. *Top*: orbital-plane snapshot at $t = 6.90$ ms. The $\rho = 10^{11} \text{ g cm}^{-3}$ contour outlines the high-density bulk of each NS. The in-plane axes indicate the line connecting the COMs and the perpendicular direction within the orbital plane. *Bottom*: inspiral evolution of the deformation measure $\eta(t)$ of both merging stars for the same two runs.

remnant. The location of this peak shifts systematically with the effective mass parameters, with typical variations of order $\Delta f \sim 150$ Hz across the explored thermal EOS parameter space at fixed cold EOS. Subdominant spectral features, related to secondary mode couplings, also show parameter dependence, although at lower amplitudes.

Whether such thermal effects can be disentangled observationally remains to be seen, but it will definitely

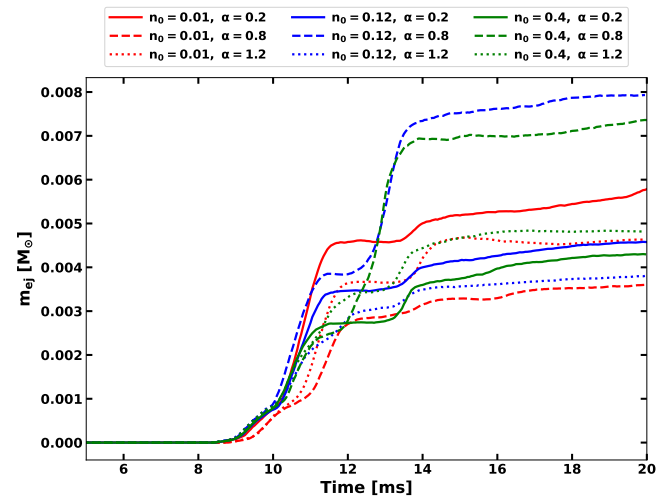


FIG. 11. Time evolution of the dynamical ejecta mass for different thermal EOS parameterizations (n_0, α) at 2×10^6 particles.

be challenging since the effects can compete with other physical processes related to magnetic field evolution and neutrino emission. Future gravitational-wave detectors, including Advanced LIGO A+ and third-generation facilities, are expected to access the dominant post-merger peak frequency. In combination with inspiral constraints on the cold EOS, post-merger spectroscopy may therefore provide a path toward probing the finite-temperature sector of dense matter. A quantitative assessment will require higher-resolution simulations, improved waveform modeling, and dedicated statistical analyses.

IV. CONCLUSION

In this paper we have presented a substantial methodological update of the Lagrangian numerical relativity code `SPHINCS_BSSN`. We abandoned our earlier convention of measuring all energies in units of the baryon rest-mass energy and now use standard numerical relativity units. More importantly, we have implemented constraint-damping terms in the BSSN spacetime evolution, closely following recent developments proposed in an Eulerian context [67]. We demonstrated that this modification reduces Hamiltonian-constraint violations by more than an order of magnitude at essentially no additional computational cost. Most importantly from a physical perspective, we implemented a finite-temperature extension of cold equations of state based on Fermi liquid theory, following the framework introduced by Raithel et al. [70, 84]. This approach replaces the commonly used ideal gas prescription with a physics-based treatment of thermal energy and pressure as a function of density, temperature, and arbitrary proton fraction, while retaining full analytic control and avoiding the computational overhead and potential ro-

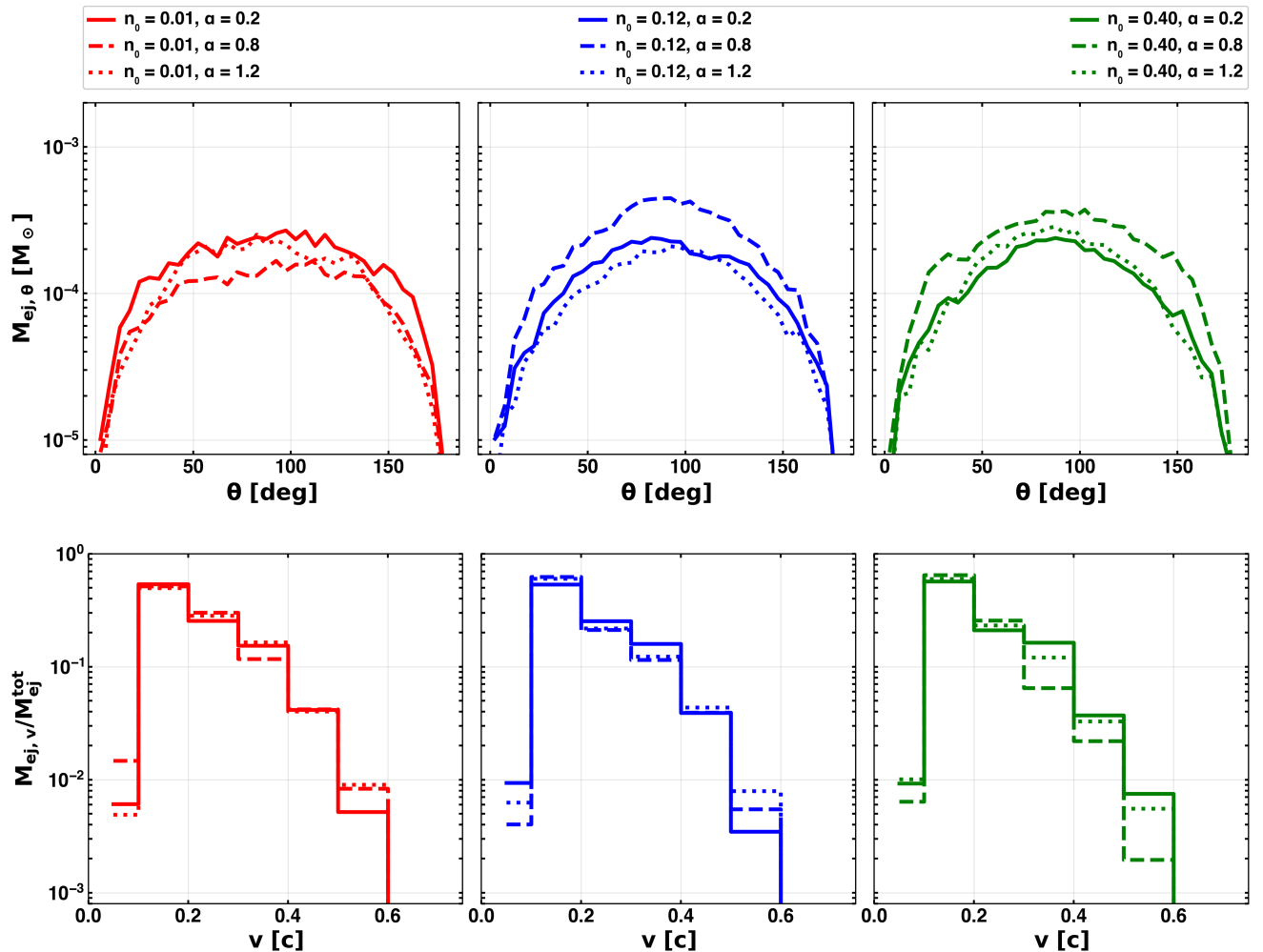


FIG. 12. Angular (top) and velocity-bin (bottom) ejecta profiles for different (n_0, α) . Both panels show only minor variations across the parameter space.

bustness issues associated with tabulated EOSs.

Using a set of fully general relativistic merger simulations, we demonstrated that the new thermal EOS implementation produces temperature distributions, and remnant structures in good qualitative agreement with previous studies employing tabulated finite-temperature EOSs. During the inspiral phase, we find that the neutron-star cores remain effectively cold, while tidal interactions heat the low-density surface layers to temperatures of order ~ 1 MeV. In the present simulations, this surface heating leads to small differences in the late-inspiral gravitational-wave phase evolution and merger time. During the merger, peak temperatures locally reach close to 100 MeV during the strongest compression phase, but the remnant subsequently settles into a new configuration with a moderately hot core (~ 10 MeV) surrounded by hotter (~ 30 MeV) surface layers, consistent with results reported in the literature.

By systematically varying the parameters that control the density dependence of the Dirac effective mass, we

explored uncertainties in the degenerate thermal sector. We found that these parameters mainly rescale the total thermal energy and the amount of dynamical ejecta, which can vary by up to a factor of two across the explored range. In contrast, the angular and velocity structure of the ejecta remain essentially unchanged. Thermal effects leave a visible imprint on the post-merger phase. In particular, we find systematic shifts of order ~ 150 Hz in the dominant post-merger spectral peak when varying the thermal EOS parameters at fixed cold EOS. While these shifts are subdominant compared to changes induced by different cold EOSs, it remains to be seen whether they can be measured observationally. Future gravitational-wave detectors, such as Advanced LIGO A+ and third-generation facilities, are expected to access the post-merger peak frequency, providing a potential avenue for confronting such thermal effects with observations.

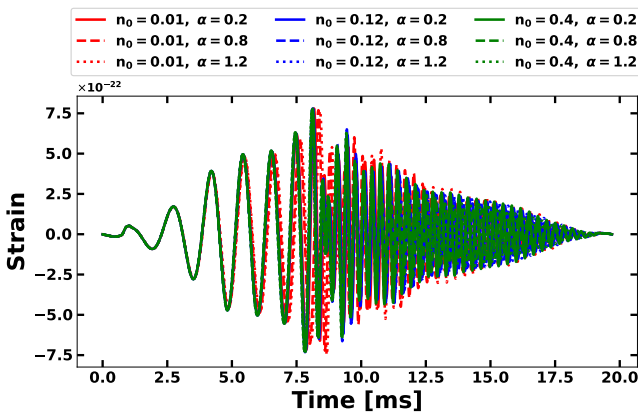


FIG. 13. Plus polarization of the $(2,2)$ mode of the gravitational-wave strain from simulations with 2×10^6 particles for different thermal EOS parameterizations (n_0, α). The inspiral portions overlap nearly perfectly, while post-merger oscillations show modest but systematic differences in phase evolution and damping.

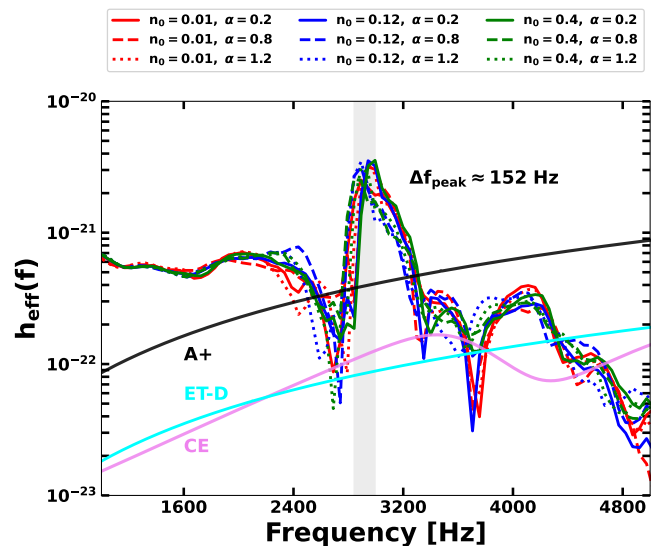


FIG. 14. Effective amplitude spectra corresponding to the waveforms in Fig. 13, compared with Advanced LIGO A+, Einstein telescope (ET), and Cosmic Explorer (CE) design sensitivities (40 Mpc). All models display a dominant kHz peak associated with the fundamental quadrupolar mode of the remnant. Thermal EOS variations induce few-percent shifts in the peak frequency and alter the prominence of secondary features.

ACKNOWLEDGEMENTS

BB and SR acknowledge the support from the Knut and Alice Wallenberg Foundation under grant Dnr. KAW 2019.0112, the Deutsche Forschungsgemeinschaft (DFG, German Research Foundation) under Germany's Excellence Strategy – EXC 2121 “Quantum Universe” – 390833306. BB was further supported by the Alexander von Humboldt Foundation through a Humboldt Research Fellowship for Postdoctoral Researchers. SR has additionally been supported by the Swedish Research Council (VR) under grant number 2020-05044, by the research environment grant “Gravitational Radiation and Electromagnetic Astrophysical Transients” (GREAT) funded by the Swedish Research Council (VR) under Dnr 2016-06012, and by the European Research Council (ERC) Advanced Grant INSPIRATION under the European Union’s Horizon 2020 research and innovation programme (Grant agreement No. 101053985) which also supports LS.

The calculations were performed in part at the NHR Center NHR@ZIB, jointly supported by the Federal Ministry of Education and Research and the state governments participating in the NHR (www.nhr-verein.de/unser-partner), at the SUNRISE HPC facility supported by the Technical Division at the Department of Physics, Stockholm University, and on the HUMMEL2 cluster funded by the Deutsche Forschungsgemeinschaft (498394658). Special thanks go to Mikica Kocic (SU), Thomas Oregis and Hinnek Stüben (both UHH) for their excellent support. Portions of this research were conducted with high performance computational resources provided by the Louisiana Optical Network Infrastructure (<http://www.loni.org>).

[1] M. Alcubierre, *Introduction to 3+1 Numerical Relativity* (Oxford University Press, 2008).

[2] T. W. Baumgarte and S. L. Shapiro, *Numerical Relativity: Solving Einstein's Equations on the Computer*, edited by Baumgarte, T. W. & Shapiro, S. L. (Cambridge University Press, ISBN: 9780521514071, Cambridge, 2010).

[3] Carles Bona, Carlos Palenzuela-Luque, and Carles Bona-Casas, *Elements of Numerical Relativity and Relativistic Hydrodynamics: From Einstein's Equations to Astrophysical Simulations* (Springer Publishing Company, Incorporated, 2011).

[4] L. Rezzolla and O. Zanotti, *Relativistic Hydrodynamics* (Oxford University Press, 2013. ISBN-10: 0198528906; ISBN-13: 978-0198528906, 2013).

[5] Masaru Shibata, *Numerical Relativity* (World Scientific, 2016).

[6] J. M. Lattimer, “The Nuclear Equation of State and Neutron Star Masses,” *Annual Review of Nuclear and Particle Science* **62**, 485–515 (2012), arXiv:1305.3510 [nucl-th].

[7] Gordon Baym, Tetsuo Hatsuda, Toru Kojo, Philip D. Powell, Yifan Song, and Tatsuyuki Takatsuka, “From hadrons to quarks in neutron stars: a review,” *Reports on Progress in Physics* **81**, 056902 (2018), arXiv:1707.04966 [astro-ph.HE].

[8] D.J. Price and S. Rosswog, “Producing ultra-strong magnetic fields in neutron star mergers,” *Science* **312**, 719 (2006).

[9] M. Anderson, E. W. Hirschmann, L. Lehner, S. L. Liebling, P. M. Motl, D. Neilsen, C. Palenzuela, and J. E. Tohline, “Magnetized Neutron-Star Mergers and Gravitational-Wave Signals,” *Physical Review Letters* **100**, 191101 (2008), arXiv:0801.4387 [gr-qc].

[10] L. Rezzolla, B. Giacomazzo, L. Baiotti, J. Granot, C. Kouveliotou, and M. A. Aloy, “The Missing Link: Merging Neutron Stars Naturally Produce Jet-like Structures and Can Power Short Gamma-ray Bursts,” *ApJL* **732**, L6 (2011), arXiv:1101.4298 [astro-ph.HE].

[11] J. Zrake and A. I. MacFadyen, “Magnetic Energy Production by Turbulence in Binary Neutron Star Mergers,” *ApJL* **769**, L29 (2013), arXiv:1303.1450 [astro-ph.HE].

[12] K. Kiuchi, P. Cerdá-Durán, K. Kyutoku, Y. Sekiguchi, and M. Shibata, “Efficient magnetic-field amplification due to the Kelvin-Helmholtz instability in binary neutron star mergers,” *Phys. Rev. D* **92**, 124034 (2015), arXiv:1509.09205 [astro-ph.HE].

[13] Carlos Palenzuela, Ricard Aguilera-Miret, Federico Carrasco, Riccardo Ciolfi, Jay Vijay Kalinani, Wolfgang Kastaun, Borja Miñano, and Daniele Viganò, “Turbulent magnetic field amplification in binary neutron star mergers,” *Phys. Rev. D* **106**, 023013 (2022), arXiv:2112.08413 [gr-qc].

[14] Ricard Aguilera-Miret, Daniele Viganò, and Carlos Palenzuela, “Universality of the Turbulent Magnetic Field in Hypermassive Neutron Stars Produced by Binary Mergers,” *ApJL* **926**, L31 (2022), arXiv:2112.08406 [gr-qc].

[15] Ricard Aguilera-Miret, Carlos Palenzuela, Federico Carrasco, Stephan Rosswog, and Daniele Viganò, “Delayed jet launching in binary neutron star mergers with realistic initial magnetic fields,” *Phys. Rev. D* **110**, 083014 (2024), arXiv:2407.20335 [astro-ph.HE].

[16] Kenta Kiuchi, Alexis Reboul-Salze, Masaru Shibata, and Yuichiro Sekiguchi, “A large-scale magnetic field produced by a solar-like dynamo in binary neutron star mergers,” *Nature Astronomy* **8**, 298–307 (2024), arXiv:2306.15721 [astro-ph.HE].

[17] Ricard Aguilera-Miret, Jan-Erik Christian, Stephan Rosswog, and Carlos Palenzuela, “Robustness of Magnetic Field Amplification in Neutron Star Mergers,” arXiv e-prints , arXiv:2504.10604 (2025), arXiv:2504.10604 [astro-ph.HE].

[18] S. Rosswog and M. Liebendörfer, “High-resolution calculations of merging neutron stars - II. Neutrino emission,” *MNRAS* **342**, 673–689 (2003).

[19] L. Dessart, C. D. Ott, A. Burrows, S. Rosswog, and E. Livne, “Neutrino Signatures and the Neutrino-Driven Wind in Binary Neutron Star Mergers,” *ApJ* **690**, 1681–1705 (2009).

[20] Y. Sekiguchi, K. Kiuchi, K. Kyutoku, M. Shibata, and K. Taniguchi, “Dynamical mass ejection from the merger of asymmetric binary neutron stars: Radiation-hydrodynamics study in general relativity,” ArXiv e-prints (2016), arXiv:1603.01918 [astro-ph.HE].

[21] David Radice, Albino Perego, Kenta Hotokezaka, Steven A. Fromm, Sebastiano Bernuzzi, and Luke F. Roberts, “Binary Neutron Star Mergers: Mass Ejection, Electromagnetic Counterparts, and Nucleosynthesis,” *ApJ* **869**, 130 (2018), arXiv:1809.11161 [astro-ph.HE].

[22] Francois Foucart, “Neutrino transport in general relativistic neutron star merger simulations,” *Living Reviews in Computational Astrophysics* **9**, 1 (2023), arXiv:2209.02538 [astro-ph.HE].

[23] H. C. Das, Ankit Kumar, and S. K. Patra, “Dark matter admixed neutron star as a possible compact component in the GW190814 merger event,” *Phys. Rev. D* **104**, 063028 (2021), arXiv:2109.01853 [astro-ph.HE].

[24] Jean-François Fortin, Huai-Ke Guo, Steven P. Harris, Doojin Kim, Kuver Sinha, and Chen Sun, “Axions: From magnetars and neutron star mergers to beam dumps and BECs,” *International Journal of Modern Physics D* **30**, 2130002 (2021), arXiv:2102.12503 [hep-ph].

[25] Mattia Emma, Federico Schianchi, Francesco Pannarale, Violetta Sagun, and Tim Dietrich, “Numerical Simulations of Dark Matter Admixed Neutron Star Binaries,” *Particles* **5**, 273–286 (2022), arXiv:2206.10887 [gr-qc].

[26] Masha Baryakhtar, Regina Caputo, Djuna Croon, Kerstin Perez, Emanuele Berti, Joseph Bramante, Malte Buschmann, Richard Brito, Thomas Y. Chen, Philippa S. Cole, Adam Coogan, William E. East, Joshua W. Foster, Marios Galanis, Maurizio Giannotti, Bradley J. Kavanagh, Ranjan Laha, Rebecca K. Leane, Benjamin V. Lehmann, Gustavo Marques-Tavares, Jamie McDonald, Ken K. Y. Ng, Nirmal Raj, Laura Sagunski, Jeremy Sakstein, B. S. Sathyaprakash, Sarah Shandera, Nils Siemonsen, Olivier Simon, Kuver Sinha, Divya Singh, Rajeev Singh, Chen Sun, Ling Sun, Volodymyr Takhistov, Yu-Dai Tsai, Edoardo

Vitagliano, Salvatore Vitale, Huan Yang, and Jun Zhang, “Dark Matter In Extreme Astrophysical Environments,” arXiv e-prints , arXiv:2203.07984 (2022), arXiv:2203.07984 [hep-ph].

[27] Leor Barack, Vitor Cardoso, Samaya Nissanke, Thomas P. Sotiriou, Abbas Askar, Chris Belczynski, Gianfranco Bertone, Edi Bon, Diego Blas, Richard Brito, Tomasz Bulik, and more, “Black holes, gravitational waves and fundamental physics: a roadmap,” *Classical and Quantum Gravity* **36**, 143001 (2019), arXiv:1806.05195 [gr-qc].

[28] Bhaskar Biswas, Evangelos Smyrniotis, Ioannis Liodis, and Nikolaos Stergioulas, “Bayesian investigation of the neutron star equation of state vs gravity degeneracy,” *Phys. Rev. D* **109**, 064048 (2024), arXiv:2309.05420 [gr-qc].

[29] James M. Lattimer and Madappa Prakash, “The equation of state of hot, dense matter and neutron stars,” *Physics Reports* **621**, 127–164 (2016), arXiv:1512.07820 [astro-ph.SR].

[30] B. P. Abbott, R. Abbott, T. D. Abbott, M. R. Abernathy, F. Acernese, K. Ackley, C. Adams, T. Adams, P. Addesso, R. X. Adhikari, and et al., “GW170817: Measurements of Neutron Star Radii and Equation of State,” *Phys. Rev. Lett.* **121**, 161101 (2018), arXiv:1805.11581 [gr-qc].

[31] Bhaskar Biswas and Stephan Rosswog, “Simultaneously constraining the neutron star equation of state and mass distribution through multimessenger observations and nuclear benchmarks,” *Phys. Rev. D* **112**, 023045 (2025), arXiv:2408.15192 [astro-ph.HE].

[32] Luca Baiotti, “Gravitational waves from neutron star mergers and their relation to the nuclear equation of state,” *Progress in Particle and Nuclear Physics* **109**, 103714 (2019), arXiv:1907.08534 [astro-ph.HE].

[33] E. Symbalisty and D. N. Schramm, “Neutron Star Collisions and the r-Process,” *Astrophys. Lett.* **22**, 143 (1982).

[34] D. Eichler, M. Livio, T. Piran, and D. N. Schramm, “Nucleosynthesis, Neutrino Bursts and γ -Ray from Coalescing Neutron Stars,” *Nature* **340**, 126 (1989).

[35] S. Rosswog, M. Liebendörfer, F.-K. Thielemann, M.B. Davies, W. Benz, and T. Piran, “Mass ejection in neutron star mergers,” *A & A* **341**, 499–526 (1999).

[36] C. Freiburghaus, S. Rosswog, and F.-K. Thielemann, “R-process in neutron star mergers,” *ApJ* **525**, L121 (1999).

[37] N. R. Tanvir, A. J. Levan, C. Gonzalez-Fernandez, O. Korobkin, I. Mandel, S. Rosswog, J. Hjorth, P. D’Avanzo, and more, “The Emergence of a Lanthanide-rich Kilonova Following the Merger of Two Neutron Stars,” *ApJL* **848**, L27 (2017), arXiv:1710.05455 [astro-ph.HE].

[38] D. Kasen, B. Metzger, J. Barnes, E. Quataert, and E. Ramirez-Ruiz, “Origin of the heavy elements in binary neutron-star mergers from a gravitational-wave event,” *Nature* **551**, 80–84 (2017), arXiv:1710.05463 [astro-ph.HE].

[39] Iair Arcavi, Griffin Hosseinzadeh, D. Andrew Howell, Curtis McCully, Dovi Poznanski, Daniel Kasen, Jennifer Barnes, Michael Zaltzman, Sergiy Vasyliev, Dan Maoz, and Stefano Valenti, “Optical emission from a kilonova following a gravitational-wave-detected neutron-star merger,” *Nature (London)* **551**, 64–66 (2017), arXiv:1710.05843 [astro-ph.HE].

[40] S. Rosswog, J. Sollerman, U. Feindt, A. Goobar, O. Korobkin, R. Wollaeger, C. Fremling, and M. M. Kasliwal, “The first direct double neutron star merger detection: Implications for cosmic nucleosynthesis,” *A&A* **615**, A132 (2018), arXiv:1710.05445 [astro-ph.HE].

[41] Brian D. Metzger, “Kilonovae,” *Living Reviews in Relativity* **23**, 1 (2019), arXiv:1910.01617 [astro-ph.HE].

[42] N. Gehrels, J. P. Norris, S. D. Barthelmy, J. Granot, Y. Kaneko, C. Kouveliotou, C. B. Markwardt, P. Mészáros, E. Nakar, J. A. Nousek, P. T. O’Brien, M. Page, D. M. Palmer, A. M. Parsons, P. W. A. Roming, T. Sakamoto, C. L. Sarazin, P. Schady, M. Statnikos, and S. E. Woosley, “A new γ -ray burst classification scheme from GRB060614,” *Nature* **444**, 1044–1046 (2006), arXiv:astro-ph/0610635 [astro-ph].

[43] B. Zhang, B.-B. Zhang, E.-W. Liang, N. Gehrels, D. N. Burrows, and P. Meszaros, “Making a Short Gamma-Ray Burst from a Long One: Implications for the Nature of GRB 060614,” *ApJL* **655**, L25–L28 (2007), astro-ph/0612238.

[44] E. Troja, H. van Eerten, B. Zhang, G. Ryan, L. Piro, R. Ricci, B. O’Connor, M. H. Wieringa, S. B. Cenko, and T. Sakamoto, “A thousand days after the merger: Continued X-ray emission from GW170817,” *Mon. not. RAS.*, **498**, 5643–5651 (2020), arXiv:2006.01150 [astro-ph.HE].

[45] Jillian C. Rastinejad, Benjamin P. Gompertz, Andrew J. Levan, Wen-fai Fong, Matt Nicholl, Gavin P. Lamb, Daniele B. Malesani, Anya E. Nugent, and more, “A kilonova following a long-duration gamma-ray burst at 350 Mpc,” *Nature* **612**, 223–227 (2022), arXiv:2204.10864 [astro-ph.HE].

[46] Yu-Han Yang, Eleonora Troja, Brendan O’Connor, Chris L. Fryer, Myungshin Im, Joe Durbak, and more, “A lanthanide-rich kilonova in the aftermath of a long gamma-ray burst,” *Nature* **626**, 742–745 (2024), arXiv:2308.00638 [astro-ph.HE].

[47] Andrew J. Levan, Benjamin P. Gompertz, Om Sharan Salafia, Mattia Bulla, Eric Burns, Kenta Hotokezaka, and more, “Heavy-element production in a compact object merger observed by JWST,” *Nature* **626**, 737–741 (2024), arXiv:2307.02098 [astro-ph.HE].

[48] B.F. Schutz, “Determining the hubble constant from gravitational wave observations,” *Nature* **323**, 310 (1986).

[49] Daniel E. Holz and Scott A. Hughes, “Using Gravitational-Wave Standard Sirens,” *Astrophys. J.* **629**, 15–22 (2005), arXiv:astro-ph/0504616 [astro-ph].

[50] Samaya Nissanke, Daniel E. Holz, Scott A. Hughes, Neal Dalal, and Jonathan L. Sievers, “Exploring Short Gamma-ray Bursts as Gravitational-wave Standard Sirens,” *ApJ* **725**, 496–514 (2010), arXiv:0904.1017 [astro-ph.CO].

[51] J. J. Monaghan, “Smoothed particle hydrodynamics,” *Reports on Progress in Physics* **68**, 1703–1759 (2005).

[52] S. Rosswog, “Astrophysical smooth particle hydrodynamics,” *New Astronomy Reviews* **53**, 78–104 (2009).

[53] S. Rosswog, “SPH Methods in the Modelling of Compact Objects,” *Living Reviews of Computational Astrophysics* (2015) **1** (2015), 10.1007/lrcap-2015-1, arXiv:1406.4224 [astro-ph.IM].

[54] S. Rosswog and P. Diener, “SPHINCS_BSSN: a general relativistic smooth particle hydrodynamics code for dy-

namical spacetimes,” *Classical and Quantum Gravity* **38**, 115002 (2021), arXiv:2012.13954 [gr-qc].

[55] S. Rosswog, O. Korobkin, A. Arcones, F.-K. Thielemann, and T. Piran, “The long-term evolution of neutron star merger remnants - I. The impact of r-process nucleosynthesis,” *MNRAS* **439**, 744–756 (2014), arXiv:1307.2939 [astro-ph.HE].

[56] José A. Font, Tom Goodale, Sai Iyer, Mark Miller, Luciano Rezzolla, Edward Seidel, Nikolaos Stergioulas, Wai-Mo Suen, and Malcolm Tobias, “Three-dimensional numerical general relativistic hydrodynamics. ii. long-term dynamics of single relativistic stars,” *Phys. Rev. D* **65**, 084024 (2002).

[57] Isabel Cordero-Carrión, Pablo Cerdá-Durán, Harald Dimmelmeier, José Luis Jaramillo, Jérôme Novak, and Eric Gourgoulhon, “Improved constrained scheme for the Einstein equations: An approach to the uniqueness issue,” *Phys. Rev. D* **79**, 024017 (2009), arXiv:0809.2325 [gr-qc].

[58] Sebastiano Bernuzzi and David Hilditch, “Constraint violation in free evolution schemes: Comparing the BSSNOK formulation with a conformal decomposition of the Z4 formulation,” *Phys. Rev. D* **81**, 084003 (2010), arXiv:0912.2920 [gr-qc].

[59] Cosimo Bambi, Yosuke Mizuno, Swarnim Shashank, and Feng Yuan, eds., ‘SPHINCS_BSSN: Numerical Relativity with Particles’ in book ‘New Frontiers in GRMHD Simulations’, Springer Series in Astrophysics and Cosmology (Springer Nature Singapore, 2025).

[60] Georges-Henri Cottet and Petros D. Koumoutsakos, *Vortex Methods* (2000).

[61] Peter Diener, Stephan Rosswog, and Francesco Torsello, “Simulating neutron star mergers with the Lagrangian Numerical Relativity code SPHINCS_BSSN,” *European Physical Journal A* **58**, 74 (2022), arXiv:2203.06478 [astro-ph.HE].

[62] S. Rosswog, “The Lagrangian hydrodynamics code MAGMA2,” *MNRAS* **498**, 4230–4255 (2020), arXiv:1911.13093 [astro-ph.IM].

[63] Stephan Rosswog, Peter Diener, and Francesco Torsello, “Thinking Outside the Box: Numerical Relativity with Particles,” *Symmetry* **14**, 1280 (2022), arXiv:2205.08130 [gr-qc].

[64] Stephan Rosswog, Francesco Torsello, and Peter Diener, “The Lagrangian Numerical Relativity code SPHINCS_BSSN_v1.0,” *Front. Appl. Math. Stat.* **9** (2023), 10.48550/arXiv.2306.06226, arXiv:2306.06226 [gr-qc].

[65] S. Rosswog, P. Diener, F. Torsello, T. M. Tauris, and N. Sarin, “Mergers of double NSs with one high-spin component: brighter kilonovae and fallback accretion, weaker gravitational waves,” *MNRAS* **530**, 2336–2354 (2024), arXiv:2310.15920 [astro-ph.HE].

[66] Stephan Rosswog, Nikhil Sarin, Ehud Nakar, and Peter Diener, “Fast dynamic ejecta in neutron star mergers,” *MNRAS* **538**, 907–924 (2025), arXiv:2411.18813 [astro-ph.HE].

[67] Zachariah B. Etienne, “Improved moving-puncture techniques for compact binary simulations,” *Phys. Rev. D* **110**, 064045 (2024), arXiv:2404.01137 [gr-qc].

[68] Constantinos Constantinou, Brian Muccioli, Madappa Prakash, and James M. Lattimer, “Thermal properties of supernova matter: The bulk homogeneous phase,” *Phys. Rev. C* **89**, 065802 (2014), arXiv:1402.6348 [astro-ph.SR].

[69] Constantinos Constantinou, Brian Muccioli, Madappa Prakash, and James M. Lattimer, “Thermal properties of hot and dense matter with finite range interactions,” *Phys. Rev. C* **92**, 025801 (2015), arXiv:1504.03982 [astro-ph.SR].

[70] Carolyn A. Raithel, Feryal Özel, and Dimitrios Psaltis, “Finite-temperature extension for cold neutron star equations of state,” *Astrophys. J.* **875**, 12 (2019), arXiv:1902.10735 [astro-ph.HE].

[71] Carolyn A. Raithel, Vasileios Paschalidis, and Feryal Özel, “Realistic finite-temperature effects in neutron star merger simulations,” *Phys. Rev. D* **104**, 063016 (2021), arXiv:2104.07226 [astro-ph.HE].

[72] G. Baym, *Landau Fermi-Liquid Theory: Concepts and Applications* (Wiley, 1991).

[73] S. Rosswog, “Relativistic smooth particle hydrodynamics on a given background spacetime,” *Classical and Quantum Gravity* **27**, 114108 (2010).

[74] J. J. Monaghan and D. J. Price, “Variational principles for relativistic smoothed particle hydrodynamics,” *MNRAS* **328**, 381–392 (2001).

[75] Michael Pürrer and Carl-Johan Haster, “Gravitational waveform accuracy requirements for future ground-based detectors,” *Physical Review Research* **2**, 023151 (2020), arXiv:1912.10055 [gr-qc].

[76] Deborah Ferguson, Karan Jani, Pablo Laguna, and Deirdre Shoemaker, “Assessing the readiness of numerical relativity for LISA and 3G detectors,” *Phys. Rev. D* **104**, 044037 (2021), arXiv:2006.04272 [gr-qc].

[77] Heinz-Otto Kreiss, “Methods for the approximate solution of time dependent problems,” (1973).

[78] W. H. Press, B. P. Flannery, S. A. Teukolsky, and W. T. Vetterling, *Numerical Recipes* (Cambridge University Press, New York, 1992).

[79] Jocelyn S. Read, Benjamin D. Lackey, Benjamin J. Owen, and John L. Friedman, “Constraints on a phenomenologically parametrized neutron-star equation of state,” *Phys. Rev. D* **79**, 124032 (2009), arXiv:0812.2163 [astro-ph].

[80] “Compstar online supernova equations of state,” <https://compose.obspm.fr>, online; accessed 16 October 2025.

[81] S. Shankar, S. Rosswog, and P. Diener, “Conservative-to-primitive recovery for tabulated equations of state in SPHINCS_BSSN,” to be submitted (2026).

[82] Bao-An Li, Wen-Jun Guo, and Zhaozhong Shi, “Effects of the kinetic symmetry energy reduced by short-range correlations in heavy-ion collisions at intermediate energies,” *Phys. Rev. C* **91**, 044601 (2015), arXiv:1408.6415 [nucl-th].

[83] D. Blaschke, D. E. Alvarez-Castillo, and T. Klähn, “Universal symmetry energy contribution to the neutron star equation of state,” arXiv e-prints , arXiv:1604.08575 (2016), arXiv:1604.08575 [nucl-th].

[84] Carolyn A. Raithel, *Constraining the neutron star equation of state with astrophysical observables*, Ph.D. thesis, University of Arizona (2020).

[85] Elias R. Most and Carolyn A. Raithel, “Impact of the nuclear symmetry energy on the post-merger phase of a binary neutron star coalescence,” *Phys. Rev. D* **104**, 124012 (2021), arXiv:2107.06804 [astro-ph.HE].

[86] Andrew W. Steiner, Matthias Hempel, and Tobias Fischer, “Core-collapse supernova equations of state based

on neutron star observations,” *Astrophys. J.* **774**, 17 (2013), arXiv:1207.2184 [astro-ph.SR].

[87] Constantinos Constantinou, Brian Muccioli, Madappa Prakash, and James M. Lattimer, “Degenerate limit thermodynamics beyond leading order for models of dense matter,” *Annals Phys.* **363**, 533–555 (2015), arXiv:1507.07874 [nucl-th].

[88] Jocelyn S. Read, Benjamin D. Lackey, Benjamin J. Owen, and John L. Friedman, “Constraints on a phenomenologically parameterized neutron-star equation of state,” *Phys. Rev. D* **79**, 124032 (2009), arXiv:0812.2163 [astro-ph].

[89] CJF Ridders, “Accurate computation of $f'(x)$ and $f''(x)$,” *Advances in Engineering Software* (1978) **4**, 75–76 (1982).

[90] William H Press, Saul A Teukolsky, William T Vetterling, and Brian P Flannery, “Numerical recipes in c. second,” New York, Press Syndicate of the University of Cambridge (1992).

[91] L. Engvik, E. Osnes, M. Hjorth-Jensen, G. Bao, and E. Ostgaard, “Asymmetric Nuclear Matter and Neutron Star Properties,” *ApJ* **469**, 794 (1996), arXiv:nucl-th/9509016 [nucl-th].

[92] Bhaskar Biswas, “Bayesian Model Selection of Neutron Star Equations of State Using Multi-messenger Observations,” *Astrophys. J.* **926**, 75 (2022), arXiv:2106.02644 [astro-ph.HE].

[93] L. Jens Papenfort, Samuel D. Tootle, Philippe Grandclément, Elias R. Most, and Luciano Rezzolla, “New public code for initial data of unequal-mass, spinning compact-object binaries,” *Phys. Rev. D* **104**, 024057 (2021), arXiv:2103.09911 [gr-qc].

[94] P. Hammond, I. Hawke, and N. Andersson, “Thermal aspects of neutron star mergers,” *Phys. Rev. D* **104**, 103006 (2021), arXiv:2108.08649 [astro-ph.HE].

[95] F. Gittins, R. Matur, N. Andersson, and I. Hawke, “Problematic systematics in neutron-star merger simulations,” *Phys. Rev. D* **111**, 023049 (2025), arXiv:2409.13468 [gr-qc].

[96] Carolyn A. Raithel, Pedro Espino, and Vasileios Paschalidis, “Finite-temperature effects in dynamical spacetime binary neutron star merger simulations: validation of the parametric approach,” *MNRAS* **516**, 4792–4804 (2022), arXiv:2206.14838 [astro-ph.HE].

[97] Carolyn A. Raithel and Vasileios Paschalidis, “Influence of stellar compactness on finite-temperature effects in neutron star merger simulations,” *Phys. Rev. D* **108**, 083029 (2023), arXiv:2306.13144 [astro-ph.HE].

[98] Albino Perego, Sebastiano Bernuzzi, and David Radice, “Thermodynamics conditions of matter in neutron star mergers,” *European Physical Journal A* **55**, 124 (2019), arXiv:1903.07898 [gr-qc].

[99] Tanja Hinderer, Benjamin D. Lackey, Ryan N. Lang, and Jocelyn S. Read, “Tidal deformability of neutron stars with realistic equations of state and their gravitational wave signatures in binary inspiral,” *Phys. Rev. D* **81**, 123016 (2010), arXiv:0911.3535 [astro-ph.HE].

[100] L. Barsotti, P. Fritschel, M. Evans, and S. Gras, *Updated Advanced LIGO sensitivity design curve*, Tech. Rep. (No. LIGO-T1800044, 2018).

[101] Michele Maggiore *et al.*, “Science Case for the Einstein Telescope,” *JCAP* **03**, 050 (2020), arXiv:1912.02622 [astro-ph.CO].

[102] David Reitze *et al.*, “Cosmic Explorer: The U.S. Contribution to Gravitational-Wave Astronomy beyond LIGO,” *Bull. Am. Astron. Soc.* **51**, 035 (2019), arXiv:1907.04833 [astro-ph.IM].